

**Title: Ocean Acidification and the Permo-Triassic Mass Extinction**

**Authors:** Clarkson, M.O.<sup>1\*</sup>; Kasemann, S.A.<sup>2</sup>; Wood, R.<sup>1</sup>; Lenton, T.M.<sup>3</sup>; Daines, S.J.<sup>3</sup>; Richoz, S.<sup>4</sup>; Ohnemüller, F.<sup>2</sup>; Meixner, A.<sup>2</sup>; Poulton, S.W.<sup>5</sup> and Tipper, E.T.<sup>6</sup>

**Affiliations:**

<sup>1</sup>. School of Geosciences, University of Edinburgh, West Mains Road, Edinburgh, EH9 3JW, UK

<sup>2</sup>. Faculty of Geosciences and MARUM-Center for Marine Environmental Sciences, University of Bremen, 28334 Bremen, Germany

<sup>3</sup>. College of Life and Environmental Sciences, University of Exeter, Laver Building, North Parks Road, Exeter, EX4 4QE, UK.

<sup>4</sup>. Institute of Earth Sciences, University of Graz, Heinrichstraße 26, 8010 Graz, Austria

<sup>5</sup>. School of Earth and Environment, University of Leeds, Leeds, LS2 9JT, UK

<sup>6</sup>. Dept. of Earth Sciences, University of Cambridge, Downing Street, Cambridge, CB2 3EQ, UK

\*Correspondence to: matthew.clarkson@otago.ac.nz

Current address: Department of Chemistry, University of Otago, Union Street, Dunedin, 9016, PO Box 56, New Zealand.

**Abstract:** Ocean acidification triggered by Siberian Trap volcanism has been implicated as a kill mechanism for the Permo-Triassic mass extinction, but evidence for an acidification event remains inconclusive. To address this, we present a high resolution seawater pH record across this interval, utilizing boron isotope data combined with a quantitative modeling approach. In the latest Permian, the alkalinity of the ocean increased, priming the Earth system with a low level of atmospheric CO<sub>2</sub> and a high ocean buffering capacity. The first phase of extinction was

coincident with a slow injection of isotopically light carbon into the atmosphere-ocean, but the ocean was well-buffered such that ocean pH remained stable. During the second extinction pulse, however, a rapid and large injection of carbon overwhelmed the buffering capacity of the ocean, causing an abrupt and short-lived acidification event that drove the preferential loss of heavily calcified marine biota.

**One Sentence Summary:** Ocean acidification caused the second phase of mass extinction in the Permo-Triassic, due to a rapid and large injection of carbon which overwhelmed the buffering capacity of the ocean.

**Main Text:** The Permian Triassic Boundary (PTB) mass extinction, at ~ 252 Ma, represents the most catastrophic loss of biodiversity in geological history, and played a major role in dictating the subsequent evolution of modern ecosystems (1). The end-Permian extinction event spans ~60 kyrs (2) and can be resolved into two distinct marine extinction pulses, with the respective kill mechanisms appearing to be ecologically selective (3). The first occurred in the latest Permian (Extinction Pulse 1; EP1) and was followed by an interval of temporary recovery before the second pulse (EP2) which occurred in the earliest Triassic. The direct cause of the mass extinction is widely debated with a diverse range of overlapping mechanisms proposed, including widespread water column anoxia (4), euxinia (5), global warming (6) and ocean acidification (7).

Models of PTB ocean acidification suggest that a massive, and rapid, release of CO<sub>2</sub> from Siberian Trap volcanism, acidified the ocean (7). Indirect evidence for acidification comes from the interpretation of faunal turnover records (3, 8), potential dissolution surfaces (9) and Ca

47 isotope data (7). A rapid input of carbon is also potentially recorded in the negative carbon  
48 isotope excursion (CIE) that characterizes the PTB (10, 11) . The interpretation of these records  
49 is, however, debated (12), and of great importance to understanding the current threat of  
50 anthropogenically-driven ocean acidification (11).

51         Here, we test the ocean acidification hypothesis by presenting a novel proxy record of  
52 ocean pH across the PTB, using the boron isotope composition of marine carbonates ( $\delta^{11}\text{B}_{\text{carb}}$ )  
53 (SM sections 2 to 4). We then employ a carbon cycle model (SM sections 3 to 5) to explore  
54 ocean carbonate chemistry and pH scenarios that are consistent with our  $\delta^{11}\text{B}$  data and published  
55 records of carbon cycle disturbance and environmental conditions. The quantitative model uses  
56 previous estimates for background Early Permian conditions (13) suggesting either high  $p\text{CO}_2$   
57 ( $\text{CO}_2\text{Hi}$ : ~10 PAL, pH ~7.5  $\delta^{11}\text{B}_{\text{SW}}$  ~36.8‰), or low  $p\text{CO}_2$  ( $\text{CO}_2\text{Lo}$ : ~3 PAL, pH ~8,  $\delta^{11}\text{B}_{\text{SW}}$   
58 ~34‰) (see SM sections 5 and 6 for further details). Through this combined geochemical,  
59 geological and modelling approach we are able to produce an envelope that encompasses the  
60 most realistic range in pH, which then allows us to resolve three distinct chronological phases of  
61 carbon cycle perturbation, each with very different environmental consequences for the Late  
62 Permian-Early Triassic Earth system.

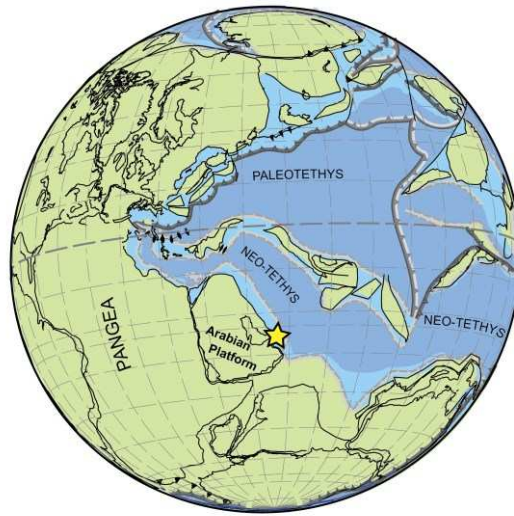
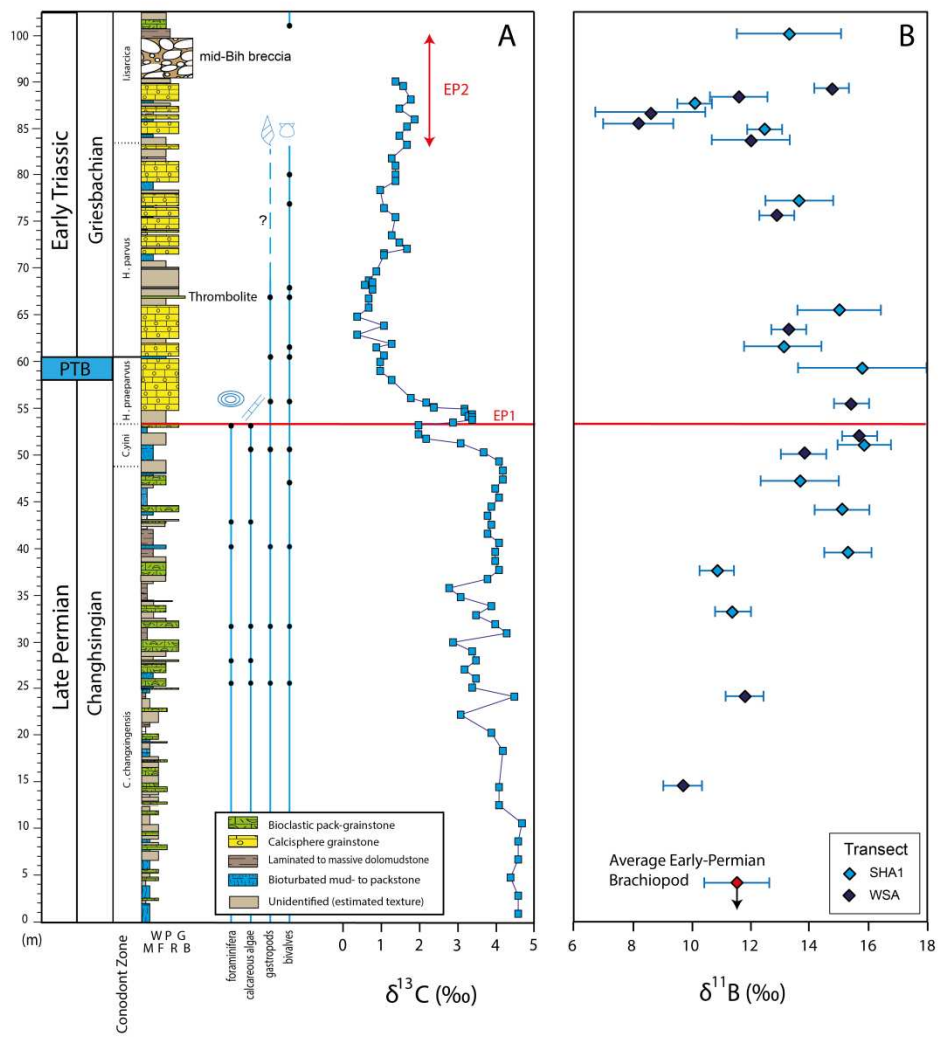


Figure 1

Figure 2

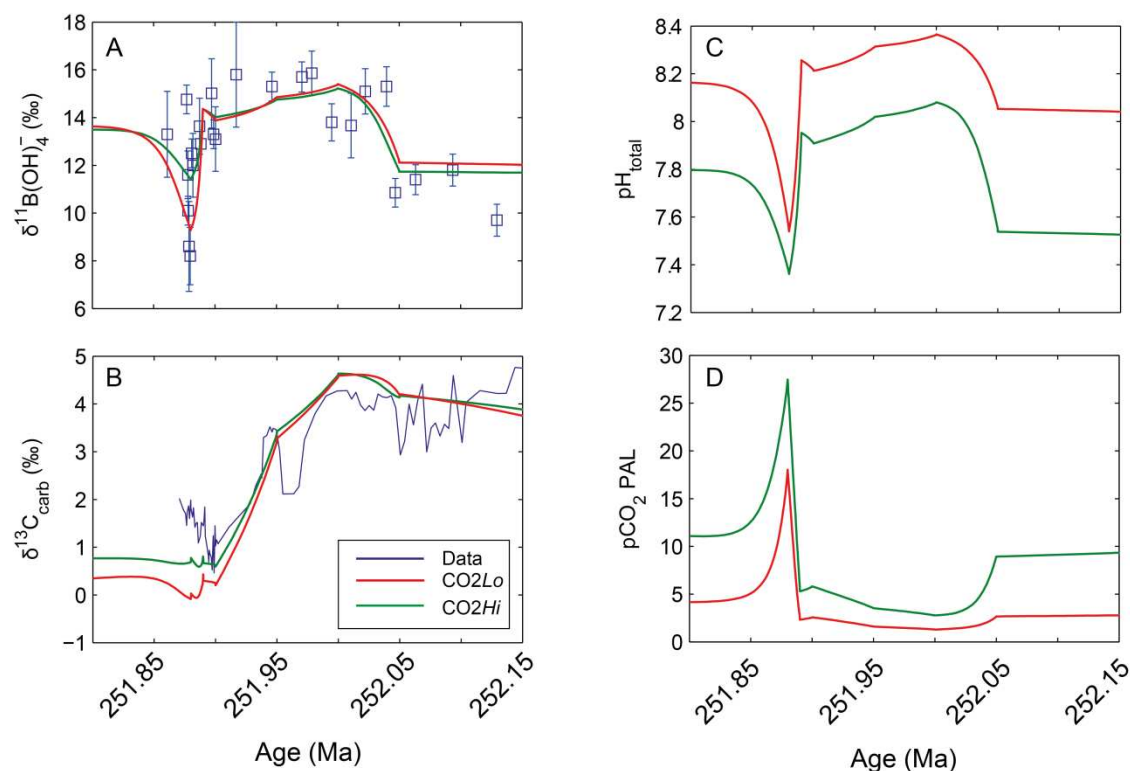


We analyzed boron isotope data from two complementary transects in a shallow marine, open water carbonate succession from the United Arab Emirates (U.A.E.), where depositional facies and  $\delta^{13}\text{C}_{\text{carb}}$  are well constrained (14) (see SM sections 1 and 2). During the Permian-Triassic the U.A.E formed an expansive carbonate platform that remained connected to the central Neo-Tethyan Ocean (15) (Fig 1). The run-up to PTB in the Tethys is characterized by two negative  $\delta^{13}\text{C}$  excursions interrupted by a short-term positive event (10). There is no consensus as to the cause of this rebound event and so we focus on the broader  $\delta^{13}\text{C}$  trend. Our  $\delta^{13}\text{C}$  transect (Fig. 2) starts in the Changhsingian with a gradual decreasing trend, interrupted by the first negative shift in  $\delta^{13}\text{C}$  at EP1 (at 53 m or ~251.96 Ma, Fig. 2). This is followed by the minor positive ‘rebound’ event (at 54 m or ~251.95 Ma, Fig. 2) prior to the minima of the second phase of the negative CIE (58-60 m or ~251.92 Ma, Figs. 2 and 3) that marks the PTB itself. After the CIE minimum,  $\delta^{13}\text{C}$  gradually increases to ~1.8‰ and remains relatively stable during earliest Triassic and across EP2.

Our boron isotope transect shows a quite different pattern.  $\delta^{11}\text{B}$  is persistently low (Fig. 2), at the start of our record during the late-Changhsingian (Late Permian), with an average of  $10.9 \pm 0.9\text{‰}$  ( $1\sigma$ ). This is in agreement with  $\delta^{11}\text{B}$  values (average of  $10.6 \pm 0.6\text{‰}$ ,  $1\sigma$ ) reported for early-Permian brachiopods (16). Further up section (at ~40 m or ~252.04 Ma, Fig. 2), there is a stepped increase in  $\delta^{11}\text{B}$  to 15.3‰, and by implication an increase in ocean pH of ~0.4-0.5 pH units (Fig. 3). Then  $\delta^{11}\text{B}$  values remain relatively stable, scattering around 14.8‰ ( $\pm 1.0$ ,  $1\sigma$ ) and implying variations within 0.1-0.2 pH units, into the Early Griesbachian (Early Triassic) and hence across EP1 and the period of carbon cycle disturbance (Figs. 2 and 3).

After  $\delta^{13}\text{C}$  had increased and stabilized (at ~85 m or ~251.88 Ma, Fig. 2),  $\delta^{11}\text{B}$  begins to decrease rapidly to 8.2‰, implying a sharp drop in pH of ~0.6-0.7 pH units. The  $\delta^{11}\text{B}$  minimum

Figure 3



is coincident with the interval identified as EP2. This ocean acidification event is short-lived (~10 kyrs) and  $\delta^{11}\text{B}$  values quickly recover toward the more alkaline values evident during EP1 (average of ~14‰).

The initial rise in ocean pH of ~0.4-0.5 units during the Late Permian (Fig. 3) suggests a large increase in carbonate alkalinity (17). We are able to simulate the observed rise in  $\delta^{11}\text{B}$  and pH through different model combinations of increasing silicate weathering, increased pyrite deposition (18), an increase in carbonate weathering and a decrease in shallow marine carbonate depositional area (see SM section 6.1). Both silicate weathering and pyrite deposition result in a large drop in  $\text{pCO}_2$  (and temperature) for a given increase in pH and saturation state ( $\Omega$ ). There is no evidence for a large drop in  $\text{pCO}_2$ , and independent proxy data indicate only a minor temperature decrease of a few degrees C during the Changhsingian (19), suggesting that these mechanisms alone cannot explain the pH increase (see sensitivity tests in SM section 6.1).

Conversely, an increase in carbonate input or a reduction in rates of carbonate deposition both result in increases in  $\Omega$ , with a greater impact on pH per unit decrease in  $p\text{CO}_2$  and temperature (see Fig. S6).

This suggested decrease in carbonate sedimentation is consistent with the decrease in depositional shelf area that occurred due to the 2<sup>nd</sup> order regression of the Late Permian (20). With the added expansion of anoxia into shelf environments (21) this would effectively create both bottom-up and top-down pressures to reduce the area of potential carbonate sedimentation. Sea level fall also exposed carbonates to weathering (20), which would have further augmented the alkalinity influx. The pH increase event supports the  $\text{CO}_2\text{Lo}$  initialisation scenario ( $\text{CO}_2 \sim 3$  PAL, pH  $\sim 8$ ,  $\delta^{11}\text{B}_{\text{SW}} \sim 34\text{‰}$ ) as the simulated  $\text{CO}_2$  and temperature decrease is much reduced, and therefore more consistent with independent proxy data (22), compared to  $\text{CO}_2\text{Hi}$  ( $\text{CO}_2 \sim 10$  PAL, pH  $\sim 7.5$ ,  $\delta^{11}\text{B}_{\text{SW}} \sim 36.8\text{‰}$ ) (Fig. 3D).

Prior to EP1,  $\delta^{13}\text{C}_{\text{carb}}$  values begin to decrease before reaching the minimum of the globally recognized negative CIE at the PTB (Fig. 2). At this time both  $\delta^{11}\text{B}$  and ocean pH remained stable. Hypotheses to explain the negative CIE require the input of isotopically light carbon, such as from volcanism (14, 23) with the assimilation of very light organic carbon from the surrounding host rock (24), methane destabilization (22), collapse of the biological pump (15), and/or a decrease in the burial of terrestrial carbon (16). We can simulate the observed drop in  $\delta^{13}\text{C}_{\text{carb}}$ , whilst remaining within the uncertainty of the  $\delta^{11}\text{B}$  data (Fig. 3), by combining a cessation of terrestrial carbon burial with a relatively slow (50 kyr) carbon injection from any of the above sources (see section S6.2.4, Fig S8). A small source of methane ( $3.2 \times 10^{17}$  mol C with  $\delta^{13}\text{C} = -50\text{‰}$ ) gives the least change in  $\delta^{11}\text{B}$  and pH, whilst either a larger source of organic

carbon ( $\sim 6.5 \times 10^{17}$  mol C with  $\delta^{13}\text{C} = -25\text{‰}$ ) or a mixture of mantle and lighter carbon sources ( $\sim 1.3 \times 10^{18}$  mol C with  $\delta^{13}\text{C} = -12.5\text{‰}$ ) are still within the measured uncertainty in  $\delta^{11}\text{B}$ .

This relatively slow carbon addition minimises the tendency for a transient decline in surface ocean pH in an ocean that was already primed with a high  $\Omega$  and hence high buffering capacity from the Late Permian. The global presence of microbial and abiotic carbonate fabrics after EP1 (Fig. 2) (25) are indicative that this high  $\Omega$  was maintained across the CIE. The carbon injection triggers an increase in  $p\text{CO}_2$ , temperature and silicate weathering, thereby creating an additional counterbalancing alkalinity flux. This is consistent with independent proxy data (6). The alkalinity source may have been further increased through soil loss (26), the emplacement of easily-weathered Siberian Trap basalt, or the impact of acid rain (27) that would have increased weathering efficiency.

The negative  $\delta^{11}\text{B}_{\text{carb}}$  excursion at 251.88 Ma represents a calculated pH decrease of up to 0.7 pH units. It coincides with the second pulse of the extinction (Fig. 2), which preferentially affected the heavily calcifying, physiologically un-buffered and sessile organisms (3). This was also accompanied by the temporary loss of abiotic and microbial carbonates throughout the Tethys (28, 29) thereby suggesting a coeval decrease in  $\Omega$  (30). To overwhelm the buffering capacity of the ocean and decrease pH in this way requires a second, more abrupt injection of carbon to the atmosphere, yet remarkably, the acidification event occurs after the decline in  $\delta^{13}\text{C}$ , when  $\delta^{13}\text{C}$  has rebounded somewhat and is essentially stable (Fig. 2).

Unlike the first carbon injection, the lack of change in  $\delta^{13}\text{C}$  at this time rules out very  $^{13}\text{C}$ -depleted carbon sources, because no counterbalancing strongly  $^{13}\text{C}$ -enriched source exists. Instead, it requires a carbon source near  $\sim 0\text{‰}$ . A plausible scenario for this is the decarbonation of overlying carbonate host rock, into which the Siberian Traps intruded (24) or the direct

assimilation of carbonates and evaporites into the melt (31). Host carbonates would have had  $\delta^{13}\text{C} \sim +2\text{--}4\text{‰}$ , which when mixed with mantle carbon ( $\sim -5\text{‰}$ ), potentially produces a source near  $0\text{‰}$ . We can simulate the sharp drop in pH and stable  $\delta^{13}\text{C}$  values (Fig. 3) through a large and rapid carbon release of  $2 \times 10^{18}$  mol C over 10 kyr (Fig S8). This second rapid carbon release produces a sharp rise in  $p\text{CO}_2$  to  $\sim 20$  PAL and warming of  $\sim 15^\circ\text{C}$ , consistent with the observation of peak temperatures after EP1 (26). Initialization of the carbon cycle model under  $\text{CO}_2\text{Hi}$  cannot generate the magnitude of  $\delta^{11}\text{B}$  drop (Fig. 3A) because the non-linear relation between pH and  $\delta^{11}\text{B}$  fractionation sets a lower limit of  $\delta^{11}\text{B}$  at  $\sim 10\text{‰}$  in this case (Fig. S3). Thus low initial  $\text{CO}_2$  of  $\sim 3$  PAL in the late Permian ( $\text{CO}_2\text{Lo}$ ) is more consistent with the data presented here.

The documented acidification event lasted for only  $\sim 10$  kyrs. This time span is consistent with the modelled timescale required to replenish the ocean with alkalinity, as carbonate deposition is reduced and weathering is increased under higher  $p\text{CO}_2$  and global temperatures. Increased silicate weathering rates drive further  $\text{CO}_2$  drawdown resulting in stabilization (Fig. S7). High global temperature (6) and increased silicate weathering are consistent with a sudden increase in both  $^{87}\text{Sr}/^{86}\text{Sr}$  (32) and sedimentation rates (26) in the Griesbachian.

The Permo-Triassic transition was a time of extreme environmental change, and our combined data and modeling approach falsifies several mechanisms for the changes observed. Whilst the coincident stresses of anoxia, increasing temperatures, and ecosystem restructuring were important during this interval, the  $\delta^{11}\text{B}$  excursion strongly suggests that widespread ocean acidification was the driver of the second pulse of the mass extinction, and thus ultimately ended the temporary recovery (3) from the first extinction pulse. The carbon release required to drive the observed acidification event occurred at a rate comparable to the current anthropogenic

168 perturbation, but far exceeded it in expected magnitude (33). We show that such a rapid rate is  
169 critical to causing the combined synchronous decrease in both pH and saturation state that  
170 defines an ocean acidification event (11).

171

172

## 173    **References and Notes**

- 174    1.     D. H. Erwin, The Permo-Triassic Extinction. *Nature* **367**, 231-236 (1994).
- 175    2.     S. D. Burgess, S. A. Bowring, S. Z. Shen, High-precision timeline for Earth's most severe  
176     extinction. *Proceedings of the National Academy of Sciences of the United States of America*  
177     **111**, 3203-3204 (2014).
- 178    3.     H. J. Song, P. B. Wignall, J. A. Tong, Y. Hongfu, Two pulses of extinction during the Permian-  
179     Triassic crisis. *Nat. Geosci.* **6**, 52-56 (2012).
- 180    4.     P. B. Wignall, R. J. Twitchett, Oceanic anoxia and the end Permian mass extinction. *Science*  
181     **272**, 1155-1158 (1996).
- 182    5.     K. Grice, C. Q. Cao, G. D. Love, M. E. Bottcher, R. J. Twitchett, E. Grosjean, R. E. Summons, S. C.  
183     Turgeon, W. Dunning, Y. G. Jin, Photic zone euxinia during the Permian-Triassic superanoxic  
184     event. *Science* **307**, 706-709 (2005); (10.1126/science.1104323).
- 185    6.     Y. D. Sun, M. M. Joachimski, P. B. Wignall, C. B. Yan, Y. L. Chen, H. S. Jiang, L. N. Wang, X. L. Lai,  
186     Lethally Hot Temperatures During the Early Triassic Greenhouse. *Science* **338**, 366-370  
187     (2012); (10.1126/science.1224126).
- 188    7.     J. L. Payne, A. V. Turchyn, A. Paytan, D. J. DePaolo, D. J. Lehrmann, M. Y. Yu, J. Y. Wei, Calcium  
189     isotope constraints on the end-Permian mass extinction. *Proceedings of the National*  
190     *Academy of Sciences of the United States of America* **107**, 8543-8548 (2010);  
191     (10.1073/pnas.0914065107).
- 192    8.     A. H. Knoll, R. K. Barnbach, J. L. Payne, S. Pruss, W. W. Fischer, Paleophysiology and end-  
193     Permian mass extinction. *Earth and Planetary Science Letters* **256**, 295-313 (2007);  
194     (10.1016/j.epsl.2007.02.018).
- 195    9.     J. L. Payne, D. J. Lehrmann, D. Follett, M. Seibel, L. R. Kump, A. Riccardi, D. Altiner, H. Sano, J.  
196     Wei, Erosional truncation of uppermost Permian shallow-marine carbonates and  
197     implications for Permian-Triassic boundary events. *Geol. Soc. Am. Bull.* **119**, 771-784  
198     (2007); (10.1130/b26091.1).
- 199    10.    C. Korte, H. W. Kozur, Carbon-isotope stratigraphy across the Permian-Triassic boundary: A  
200     review. *Journal of Asian Earth Sciences* **39**, 215-235 (2010); (10.1016/j.jseae.2010.01.005).
- 201    11.    B. Hönisch, A. Ridgwell, D. N. Schmidt, E. Thomas, S. J. Gibbs, A. Sluijs, R. Zeebe, L. Kump, R. C.  
202     Martindale, S. E. Greene, W. Kiessling, J. Ries, J. C. Zachos, D. L. Royer, S. Barker, T. M.  
203     Marchitto, Jr., R. Moyer, C. Pelejero, P. Ziveri, G. L. Foster, B. Williams, The Geological Record  
204     of Ocean Acidification. *Science* **335**, 1058-1063 (2012); (10.1126/science.1208277).
- 205    12.    C. L. Blätter, H. C. Jenkyns, L. M. Reynard, G. M. Henderson, Significant increases in global  
206     weathering during Oceanic Anoxic Events 1a and 2 indicated by calcium isotopes. *Earth and*  
207     *Planetary Science Letters* **309**, 77-88 (2011).

208 13. Y. Cui, L. R. Kump, Global warming and the end-Permian extinction event: Proxy and  
209 modeling perspectives. *Earth-Science Reviews*, (2014);  
210 (<http://dx.doi.org/10.1016/j.earscirev.2014.04.007>).

211 14. M. O. Clarkson, S. Richoz, R. A. Wood, F. Maurer, L. Krystyn, D. J. McGurty, D. Astratti, A new  
212 high-resolution delta C-13 record for the Early Triassic: Insights from the Arabian Platform.  
213 *Gondwana Research* **24**, 233-242 (2013); (10.1016/j.gr.2012.10.002).

214 15. G. M. Stampfli, G. D. Borel, A plate tectonic model for the Paleozoic and Mesozoic  
215 constrained by dynamic plate boundaries and restored synthetic oceanic isochrons. *Earth*  
216 *and Planetary Science Letters* **196**, 17-33 (2002); (Pii s0012-821x(01)00588-  
217 x10.1016/s0012-821x(01)00588-x).

218 16. M. M. Joachimski, L. Simon, R. van Geldern, C. Lecuyer, Boron isotope geochemistry of  
219 Paleozoic brachiopod calcite: Implications for a secular change in the boron isotope  
220 geochemistry of seawater over the Phanerozoic. *Geochimica et Cosmochimica Acta* **69**, 4035-  
221 4044 (2005); (10.1016/j.gca.2004.11.017).

222 17. the alternative way to drive an increase in pH would be through a removal of carbon,  
223 however this would be evident in the  $\delta^{13}\text{C}$  record so we can rule it out.

224 18. Bacterial Sulfate Reduction (BSR) is a net source of alkalinity if the generated  $\text{H}_2\text{S}$  is buried  
225 as pyrite. Pyrite deposition is seen widely in certain setting during the Late Permian to PTB.  
226 See SI for further information.

227 19. M. M. Joachimski, X. L. Lai, S. Z. Shen, H. S. Jiang, G. M. Luo, B. Chen, J. Chen, Y. D. Sun, Climate  
228 warming in the latest Permian and the Permian-Triassic mass extinction. *Geology* **40**, 195-  
229 198 (2012); (Doi 10.1130/G32707.1).

230 20. H. Yin, H. Jiang, W. Xia, Q. Feng, N. Zhang, J. Shen, The end-Permian regression in South China  
231 and its implication on mass extinction. *Earth-Sci. Rev.* **137**, 19-33 (2014);  
232 (<http://dx.doi.org/10.1016/j.earscirev.2013.06.003>).

233 21. P. B. Wignall, R. J. Twitchett, Extent, duration, and nature of the Permian-Triassic  
234 superanoxic event. *Catastrophic Events and Mass Extinctions: Impacts and Beyond*, 395-413  
235 (2002).

236 22. E. S. Krull, G. J. Retallack,  $\delta^{13}\text{C}$  depth profiles from paleosols across the Permian-Triassic  
237 boundary: Evidence for methane release. *Geol. Soc. Am. Bull.* **112**, 1459-1472 (2000);  
238 (10.1130/0016-7606(2000)112%3c;1459:cdpfpa%3e;2.0.co;2).

239 23. C. Korte, P. Pande, P. Kalia, H. W. Kozur, M. M. Joachimski, H. Oberhaensli, Massive volcanism  
240 at the Permian-Triassic boundary and its impact on the isotopic composition of the ocean  
241 and atmosphere. *Journal of Asian Earth Sciences* **37**, 293-311 (2010);  
242 (10.1016/j.jseaes.2009.08.012).

243 24. H. Svensen, S. Planke, A. G. Polozov, N. Schmidbauer, F. Corfu, Y. Y. Podladchikov, B. Jamtveit,  
244 Siberian gas venting and the end-Permian environmental crisis. *Earth and Planetary Science*  
245 *Letters* **277**, 490-500 (2009); (10.1016/j.epsl.2008.11.015).

- 246 25. A. D. Woods, Assessing Early Triassic Paleooceanographic conditions via unusual  
247 sedimentary fabrics and features. *Earth-Sci. Rev.*, (2013);  
248 (<http://dx.doi.org/10.1016/j.earscirev.2013.08.015>).
- 249 26. T. J. Algeo, Z. Q. Chen, M. L. Fraiser, R. J. Twitchett, Terrestrial-marine teleconnections in the  
250 collapse and rebuilding of Early Triassic marine ecosystems. *Paleogeography*  
251 *Paleoclimatology Paleoecology* **308**, 1-11 (2011); (10.1016/j.paleo.2011.01.011).
- 252 27. B. A. Black, J. F. Lamarque, C. A. Shields, L. T. Elkins-Tanton, J. T. Kiehl, Acid rain and ozone  
253 depletion from pulsed Siberian Traps magmatism. *Geology* **42**, 67-70 (2014); (Doi  
254 10.1130/G34875.1).
- 255 28. A. Baud, S. Richoz, S. Pruss, The lower Triassic anachronistic carbonate facies in space and  
256 time. *Global and Planetary Change* **55**, 81-89 (2007); (10.1016/j.gloplacha.2006.06.008).
- 257 29. S. Richoz, L. Krystyn, A. Baud, R. Brandner, M. Horacek, P. Mohtat-Aghai, Permian-Triassic  
258 boundary interval in the Middle East (Iran and N. Oman): Progressive environmental  
259 change from detailed carbonate carbon isotope marine curve and sedimentary evolution.  
260 *Journal of Asian Earth Sciences* **39**, 236-253 (2010); (10.1016/j.jseaes.2009.12.014).
- 261 30. Note that the system cannot be undersaturated as this precludes the preservation of the  
262 boron isotope record.
- 263 31. B. A. Black, L. T. Elkins-Tanton, M. C. Rowe, I. U. Peate, Magnitude and consequences of  
264 volatile release from the Siberian Traps. *Earth and Planetary Science Letters* **317**, 363-373  
265 (2012); (Doi 10.1016/J.Epsl.2011.12.001).
- 266 32. C. Korte, H. W. Kozur, M. M. Joachimski, H. Strauss, J. Veizer, L. Schwark, Carbon, sulfur,  
267 oxygen and strontium isotope records, organic geochemistry and biostratigraphy across the  
268 Permian/Triassic boundary in Abadeh, Iran. *International Journal of Earth Sciences* **93**, 565-  
269 581 (2004); (Doi 10.1007/S00531-004-0406-7).
- 270 33. The imposed perturbation for the acidification event is 24000 PgC compared to the  
271 estimates of 4-5000PgC that could be generated from conventional fossil fuels. Upper  
272 estimates using unconventional fossil fuels (e.g. methane hydrates) can reach ~ 24000 PgC
- 273 34. F. Maurer, R. Martini, R. Rettori, H. Hillgartner, S. Cirilli, The geology of Khuff outcrop  
274 analogues in the Musandam Peninsula, United Arab Emirates and Oman. *GeoArabia* **14**, 125-  
275 158 (2009).
- 276 35. S. Z. Shen, C. Q. Cao, H. Zhang, S. A. Bowring, C. M. Henderson, J. L. Payne, V. I. Davydov, B.  
277 Chen, D. X. Yuan, Y. C. Zhang, W. Wang, Q. F. Zheng, High-resolution delta C-13(carb)  
278 chemostratigraphy from latest Guadalupian through earliest Triassic in South China and  
279 Iran. *Earth and Planetary Science Letters* **375**, 156-165 (2013); (Doi  
280 10.1016/J.Epsl.2013.05.020).
- 281 36. B. Koehrer, M. Zeller, T. Aigner, M. Poeppelreiter, P. Milroy, H. Forke, S. Al-Kindi, Facies and  
282 stratigraphic framework of a Khuff outcrop equivalent: Saiq and Mahil formations, Al Jabal  
283 al-Akhdar, Sultanate of Oman. *GeoArabia* **15**, 91-156 (2010).

- 284 37. S. Kasemann, A. Meixner, A. Rocholl, T. Vennemann, M. Rosner, A. K. Schmitt, M.  
285 Wiedenbeck, Boron and oxygen isotope composition of certified reference materials NIST  
286 SRM 610/612 and reference materials JB-2 and JR-2. *Geostandards Newsletter-the Journal of*  
287 *Geostandards and Geoanalysis* **25**, 405-416 (2001); (Doi 10.1111/J.1751-  
288 908x.2001.Tb00615.X).
- 289 38. J. Vogl, M. Rosner, W. Pritzkow, Development and validation of a single collector SF-ICPMS  
290 procedure for the determination of boron isotope ratios in water and food samples. *Journal*  
291 *of Analytical Atomic Spectrometry*, **26**, 861-869 (2011).
- 292 39. S. A. Kasemann, S. D. N. Schmidt, J. Bijma, J., G. L. Foster, In situ boron isotope analysis in  
293 marine carbonates and its application for foraminifera and paleo-pH. *Chemical Geology*,  
294 **260**, 138-147 (2009)
- 295 40. S. A. Kasemann, C. J. Hawkesworth, A. R. Prave, A. E. Fallick, P. N. Pearson, Boron and calcium  
296 isotope composition in Neoproterozoic carbonate rocks from Namibia: evidence for  
297 extreme environmental change. *Earth and Planetary Science Letters* **231**, 73-86 (2005); (Doi  
298 10.1016/J.Epsl.2004.12.006).
- 299 41. F. Ohnemüller, A. R. Prave, A. E. Fallick, S. A. Kasemann, Ocean acidification in the aftermath  
300 of the Marinoan glaciation. *Geology*, doi:10.1130/G35937.1 (2014).
- 301 42. P. B. Wignall, A. Hallam, Facies change and the end-Permian mass extinction in SE Sichuan,  
302 China. *Palaaios* **11**, 587-596 (1996).
- 303 43. L. Breesch, R. Swennen, B. Dewever, F. Roure, B. Vincent, Diagenesis and fluid system  
304 evolution in the northern Oman Mountains, United Arab Emirates: Implications for  
305 petroleum exploration. *GeoArabia* **16**, 111-148 (2011).
- 306 44. S. B. Jacobsen, A. J. Kaufman, The Sr, C and O isotopic evolution of Neoproterozoic seawater.  
307 *Chem. Geol.* **161**, 37-57 (1999); (Doi 10.1016/S0009-2541(99)00080-7).
- 308 45. S. A. Kasemann, A. R. Prave, A. E. Fallick, C. J. Hawkesworth, K. H. Hoffmann, Neoproterozoic  
309 ice ages, boron isotopes, and ocean acidification: Implications for a snowball Earth. *Geology*  
310 **38**, 775-778 (2010); (10.1130/g30851.1).
- 311 46. G. Paris, A. Bartolini, Y. Donnadieu, V. Beaumont, J. Gaillardet, Investigating boron isotopes  
312 in a middle Jurassic micritic sequence: Primary vs. diagenetic signal. *Chem. Geol.* **275**, 117-  
313 126 (2010); (10.1016/j.chemgeo.2010.03.013).
- 314 47. A. J. Spivack, J. M. Edmond, Boron Isotope Exchange between Seawater and the Oceanic-  
315 Crust. *Geochimica et Cosmochimica Acta* **51**, 1033-1043 (1987); (Doi 10.1016/0016-  
316 7037(87)90198-0).
- 317 48. J. Veizer, D. Ala, K. Azmy, P. Bruckschen, D. Buhl, F. Bruhn, G.A. F. Carden, A. Diener, S.  
318 Ebner, Y. Godderis, T. Jasper, C. Korte, F. Pawellek, O. Podlaha, and Strauss, H. "<sup>87</sup>Sr/<sup>86</sup>Sr,  
319  $\delta^{13}\text{C}$  and  $\delta^{18}\text{O}$  evolution of Phanerozoic seawater". *Chemical Geology* **161**: 59-88 (1999).
- 320 49. D. Lemarchand, J. Gaillardet, E. Lewin, C. J. Allegre, The influence of rivers on marine boron  
321 isotopes and implications for reconstructing past ocean pH. *Nature* **408**, 951-954 (2000).

- 322 50. A. G. Dickson, Thermodynamics of the dissociation of boric-acid in synthetic seawater from  
323 273.15-k to 318.15-k. *Deep-Sea Research Part a-Oceanographic Research Papers* **37**, 755-766  
324 (1990).
- 325 51. M. Schobben, M. M. Joachimski, D. Korn, L. Leda, C. Korte, Paleotethys seawater temperature  
326 rise and an intensified hydrological cycle following the end-Permian mass extinction.  
327 *Gondwana Research*, (2013); (<http://dx.doi.org/10.1016/j.gr.2013.07.019>).
- 328 52. J. T. Kiehl, C. A. Shields, Climate simulation of the latest Permian: Implications for mass  
329 extinction. *Geology* **33**, 757-760 (2005); (Doi 10.1130/G21654.1).
- 330 53. R. A. Locarnini, A. V. Mishonov, J. I. Antonov, T. P. Boyer, H. E. Garcia, in *NOAA Atlas NESDIS*  
331 *61*, S. Levitus, Ed. (U.S. Government Printing Office, Washington, D.C, 2006), vol. 1:  
332 Temperature.
- 333 54. P. N. Pearson, M. R. Palmer, Atmospheric carbon dioxide concentrations over the past 60  
334 million years. *Nature* **406**, 695-699 (2000).
- 335 55. G. L. Foster, Seawater pH, PCO<sub>2</sub> and [CO<sub>3</sub><sup>2-</sup>] variations in the Caribbean Sea over the last  
336 130 kyr: A boron isotope and B/Ca study of planktic foraminifera. *Earth and Planetary*  
337 *Science Letters* **271**, 254-266 (2008); (10.1016/j.epsl.2008.04.015).
- 338 56. B. Hönisch, N. G. Hemming, D. Archer, M. Siddall, J. F. McManus, Atmospheric Carbon Dioxide  
339 Concentration Across the Mid-Pleistocene Transition. *Science* **324**, 1551-1554 (2009); (Doi  
340 10.1126/Science.1171477).
- 341 57. N. G. Hemming, G. N. Hanson, Boron isotopic composition and concentration in modern  
342 marine carbonates. *Geochimica et Cosmochimica Acta* **56**, 537-543 (1992).
- 343 58. N. G. Hemming, B. Honisch, A critical review and recent advances in the boron isotope  
344 paleo-pH proxy. *Geochimica et Cosmochimica Acta* **69**, A129-A129 (2005).
- 345 59. K. Klochko, A. J. Kaufman, W. S. Yao, R. H. Byrne, J. A. Tossell, Experimental measurement of  
346 boron isotope fractionation in seawater. *Earth and Planetary Science Letters* **248**, 276-285  
347 (2006); (10.1016/j.epsl.2006.05.034).
- 348 60. E. Lewis, D. W. R. Wallace. (Oak Ridge, 1998).
- 349 61. J. W. B. Rae, G. L. Foster, D. N. Schmidt, T. Elliott, Boron isotopes and B/Ca in benthic  
350 foraminifera: Proxies for the deep ocean carbonate system. *Earth and Planetary Science*  
351 *Letters* **302**, 403-413 (2011).
- 352 62. M. Pagani, J. C. Zachos, K.H. Freeman, B. Tipple, H. Bohaty, Marked decline in atmospheric  
353 carbon dioxide concentrations during the Paleogene. *Science* **309**, 600-603 (2005)
- 354 63. A. Sanyal, M. Nugent, R. J. Reeder, J. Buma, Seawater pH control on the boron isotopic  
355 composition of calcite: Evidence from inorganic calcite precipitation experiments.  
356 *Geochimica et Cosmochimica Acta* **64**, 1551-1555 (2000).

357 64. K. Klochko, G. D. Cody, J. A. Tossell, P. Dera, A. J. Kaufman, Re-evaluating boron speciation in  
358 biogenic calcite and aragonite using B-11 MAS NMR. *Geochimica et Cosmochimica Acta* **73**,  
359 1890-1900 (2009); (10.1016/j.gca.2009.01.002).

360 65. R. A. Berner, Examination of hypotheses for the Permo-Triassic boundary extinction by  
361 carbon cycle modeling. *Proceedings of the National Academy of Sciences of the United States*  
362 *of America* **99**, 4172-4177 (2002); (10.1073/pnas.032095199).

363 66. M. R. Rampino, K. Caldeira, Major perturbation of ocean chemistry and a 'Strangelove Ocean'  
364 after the end-Permian mass extinction. *Terra Nova* **17**, 554-559 (2005); (10.1111/j.1365-  
365 3121.2005.00648.x).

366 67. J. Payne, L. Kump, Evidence for recurrent Early Triassic massive volcanism from  
367 quantitative interpretation of carbon isotope fluctuations. *Earth and Planetary Science*  
368 *Letters* **256**, 264-277 (2007); (10.1016/j.epsl.2007.01.034).

369 68. K. Caldeira, J. F. Kasting, The life span of the biosphere revisited. *Nature* **360**, 721-723  
370 (1992).

371 69. J. M. Bergman, T. M. Lenton, A. J. Watson, COPSE: A new model of biogeochemical cycling  
372 over Phanerozoic time. *American Journal of Science* **304**, (2004).

373 70. A. F. Hofmann, K. Soetaert, J. J. Middelburg, F. J. R. Meysman, AquaEnv : An Aquatic Acid-  
374 Base Modelling Environment in R. *Aquatic Geochemistry* **16**, 507-546 (2010);  
375 (10.1007/s10498-009-9084-1).

376 71. R. E. Zeebe, P. Westbrooke, A simple model for the CaCO<sub>3</sub> saturation state of the ocean: The  
377 "Strangelove," the "Neritan," and the "Cretan" Ocean. *Geochemistry Geophysics Geosystems*  
378 **4**, (2003).

379 72. J. Zhang, P. D. Quay, D. O. Wilbur, Carbon isotope fractionation during gas-water exchange  
380 and dissolution of CO<sub>2</sub>. *Geochimica et Cosmochimica Acta* **59**, 107-114 (1995).

381 73. H. D. Holland, in *Treatise on Geochemistry: Vol 6 The oceans and marine geochemistry*, H. D.  
382 Holland, K. K. Turekian, Eds. (Elsevier Academic Press, 2003), pp. 583-625.

383 74. H. Song, J. Tong, T. J. Algeo, H. Song, H. Qiu, Y. Zhu, L. Tian, S. Bates, T. W. Lyons, G. Luo, L. R.  
384 Kump, Early Triassic seawater sulfate drawdown. *Geochimica et Cosmochimica Acta* **128**,  
385 95-113 (2014); (10.1016/j.gca.2013.12.009).

386 75. G. Luo, L. R. Kump, Y. Wang, J. Tong, M. a. Arthur, H. Yang, J. Huang, H. Yin, S. Xie, Isotopic  
387 evidence for an anomalously low oceanic sulfate concentration following end-Permian mass  
388 extinction. *Earth and Planetary Science Letters* **300**, 101-111 (2010);  
389 (10.1016/j.epsl.2010.09.041).

390 76. S. Ben-Yaakov, M. B. Goldhaber, The influence of sea water composition on the apparent  
391 constants of the carbonate system. *Deep Sea Research and Oceanographic Abstracts* **20**, 87-  
392 99 (1973); (10.1016/0011-7471(73)90044-2).

393 77. R. E. Zeebe, LOSCAR: Long-term Ocean-atmosphere-Sediment CARbon cycle Reservoir Model  
394 v2.0.4. *Geoscientific Model Development* **5**, 149-166 (2012); (10.5194/gmd-5-149-2012).

- 395 78. Y. Cui, L. R. Kump, Global warming and the end-Permian extinction event: Proxy and  
396 modeling perspectives. (2014); (doi:10.1016/j.earscirev.2014.04.007).
- 397 79. Y. Cui, L. R. Kump, A. Ridgwell, Initial assessment of the carbon emission rate and climatic  
398 consequences during the end-Permian mass extinction. *Paleogeography Paleoclimatology*  
399 *Paleoecology* **389**, 128-136 (2013).
- 400 80. T. J. Algeo, K. Kuwahara, H. Sano, S. Bates, T. Lyons, E. Elswick, L. Hinnov, B. Ellwood, J.  
401 Moser, J. B. Maynard, Spatial variation in sediment fluxes, redox conditions, and productivity  
402 in the Permian–Triassic Panthalassic Ocean. *Paleogeography, Paleoclimatology, Paleoecology*  
403 **308**, 65-83 (2011); (10.1016/j.paleo.2010.07.007).
- 404 81. T. J. Algeo, R. J. Twitchett, Anomalous Early Triassic sediment fluxes due to elevated  
405 weathering rates and their biological consequences. *Geology* **38**, 1023-1026 (2010);  
406 (10.1130/g31203.1).
- 407 82. G. A. Brennecka, A. D. Herrmann, T. J. Algeo, A. D. Anbar, Rapid expansion of oceanic anoxia  
408 immediately before the end-Permian mass extinction. *Proceedings of the National Academy*  
409 *of Sciences of the United States of America* **108**, 17631-17634 (2011);  
410 (10.1073/pnas.1106039108).
- 411 83. S. E. Grasby, B. Beauchamp, Latest Permian to Early Triassic basin-to-shelf anoxia in the  
412 Sverdrup Basin, Arctic Canada. *Chem. Geol.* **264**, 232-246 (2009); (Doi  
413 10.1016/J.Chemgeo.2009.03.009).
- 414 84. C. Winguth, A. M. E. Winguth, Simulating Permian-Triassic oceanic anoxia distribution:  
415 Implications for species extinction and recovery. *Geology* **40**, 127-130 (2012);  
416 (10.1130/g32453.1).
- 417 85. T. J. Algeo, C. M. Henderson, J. N. Tong, Q. L. Feng, H. F. Yin, R. V. Tyson, Plankton and  
418 productivity during the Permian-Triassic boundary crisis: An analysis of organic carbon  
419 fluxes. *Global and Planetary Change* **105**, 52-67 (2013); (Doi  
420 10.1016/J.Gloplacha.2012.02.008).
- 421 86. E. Tziperman, I. Halevy, D. T. Johnston, A. H. Knoll, D. P. Schrag, Biologically induced  
422 initiation of Neoproterozoic snowball-Earth events. *Proceedings of the National Academy of*  
423 *Sciences of the United States of America*, 1-6 (2011); (10.1073/pnas.1016361108).
- 424 87. S. W. Poulton, D. E. Canfield, Ferruginous Conditions: A Dominant Feature of the Ocean  
425 through Earth's History. *Elements* **7**, 107-112 (2011); (10.2113/gselements.7.2.107).
- 426 88. H. Song, J. Tong, T. J. Algeo, H. Song, H. Qiu, Y. Zhu, L. Tian, S. Bates, T. W. Lyons, G. Luo, L. R.  
427 Kump, Early Triassic seawater sulfate drawdown. *Geochimica et Cosmochimica Acta*,  
428 (2013); (doi: <http://dx.doi.org/10.1016/j.gca.2013.12.009>).
- 429 89. W. S. Broecker, S. Peacock, An ecologic explanation for the Permo-Triassic carbon and sulfur  
430 isotope shifts. *Global Biogeochemical Cycles* **13**, 1167-1172 (1999).
- 431 90. G. Luo, Y. Wang, K. Grice, S. Kershaw, T. J. Algeo, X. Ruan, H. Yang, C. Jia, S. Xie, Microbial–  
432 algal community changes during the latest Permian ecological crisis: Evidence from lipid

433 biomarkers at Cili, South China. *Global and Planetary Change* **105**, 36-51 (2013);  
434 (10.1016/j.gloplacha.2012.11.015).

435 91. K. M. Meyer, M. Yu, A. B. Jost, B. M. Kelley, J. L. Payne,  $\delta^{13}\text{C}$  evidence that high primary  
436 productivity delayed recovery from end-Permian mass extinction. *Earth and Planetary*  
437 *Science Letters* **302**, 378-384 (2011); (10.1016/j.epsl.2010.12.033).

438 92. H. J. Song, J. N. Tong, Y. L. Xiong, D. Y. Sun, L. Tian, H. Y. Song, The large increase of  
439  $\delta^{13}\text{C}(\text{carb})$ -depth gradient and the end-Permian mass extinction. *Sci. China-Earth Sci.* **55**,  
440 1101-1109 (2012); (10.1007/s11430-012-4416-1).

441 93. D. E. Ogden, N. H. Sleep, Explosive eruption of coal and basalt and the end-Permian mass  
442 extinction. *Proceedings of the National Academy of Sciences of the United States of America*  
443 **109**, 59-62 (2012); (10.1073/pnas.1118675109).

444 94. M. K. Reichow, A. D. Saunders, R. V. White, M. S. Pringle, A. I. Al'Mukhamedov, A. I.  
445 Medvedev, N. P. Kirda, Ar-40/Ar-39 dates from the West Siberian Basin: Siberian flood  
446 basalt province doubled. *Science* **296**, 1846-1849 (2002).

447 95. M. B. Harfoot, J. a. Pyle, D. J. Beerling, End-Permian ozone shield unaffected by oceanic  
448 hydrogen sulphide and methane releases. *Nat. Geosci.* **1**, 247-252 (2008);  
449 (10.1038/ngeo154).

450 96. C. Ganino, N. T. Arndt, Climate changes caused by degassing of sediments during the  
451 emplacement of large igneous provinces. *Geology* **37**, 323-326 (2009);  
452 (10.1130/G25325A.1).

453

454

455

456

**Acknowledgements:** MOC acknowledges funding from the Edinburgh University Principal's Career Development Scholarship and the International Centre for Carbonate Reservoirs. RW, TL and SWP acknowledge support from NERC through the 'Co-evolution of Life and the Planet' scheme (NE/I005978). SK and FO acknowledge support from the DFG. This is a contribution to IGCP 572 with S.R. sponsored for fieldwork by the Austrian National Committee (Austrian Academy of Sciences) for IGCP. We are grateful to Rob Newton and Alex Thomas for helpful discussions, Leo Krystyn for field assistance, Florian Maurer for providing photomicrographs, and Ben Mills for assisting with model studies.

**Fig. 1:** Paleogeographic reconstruction for the Late Permian denoting the studied section Wadi Bih, in the Musandam Mountains of U.A.E that formed an extensive carbonate platform in the Neo-Tethyan Ocean. Modified from (14).

**Fig. 2:** Carbon cycle dynamics, macrofauna distribution (34), and Extinction Phase 1 (EP1) and Extinction Phase 2 interval (EP2) across the Permian Triassic Boundary for Wadi Bih, A: shallow water  $\delta^{13}\text{C}$  record (14); B: Boron isotope ( $\delta^{11}\text{B}$ ) record (propagated uncertainty given as  $2\sigma_f$ ) and average Early Permian brachiopod value ( $n=5$ ) (16). Blue symbols are for SHA1 transect, black symbols are for WSA transect. The two transects are separated by  $\sim 1\text{km}$  and facies are laterally continuous. Only *H. parvus* has been found so far in this section and the conodont zones with dashed line are identified from the  $\delta^{13}\text{C}$  record (34-36).

**Fig. 3:** Model results of carbon cycle parameters for the two end-member  $\text{CO}_2$  scenarios ( $\text{CO}_2\text{Hi}$  and  $\text{CO}_2\text{Lo}$ ). A - Model reproduced  $\delta^{11}\text{B}$  vs data. B – Modelled  $\delta^{13}\text{C}$  vs data. C – Modelled pH

480 envelope incorporating uncertainty of  $\delta^{11}\text{B}_{\text{SW}}$  and dynamic temperatures. D – calculated

481 atmospheric  $\text{CO}_2$ . See SM section 1.2 for details on age model.

482

483

484 **Supplementary Materials:**

485 Materials and Methods

486 Figures S1-S9

487 Tables S1-S10

488 References (37-96)

489

490 **Supplementary Materials**

491 **1. Materials and Methods**

492 **1.1 Sample Section**

493 Carbonate samples were obtained from a shallow-marine platform section at Wadi Bih on the  
494 Musandam Peninsula, United Arab Emirates (UAE). GPS co-ordinate for main transect in Wadi  
495 Shahha are N 025° 50' 31.7", E 056° 06' 41.7". This is a near-continuous and exclusively  
496 shallow marine carbonate succession from the late Permian and entire Early Triassic that allows  
497 analysis of a high-resolution signature in the absence of significant depth-dependent or  
498 lithological controls (14). Late Permian facies are predominantly intertidal mud-and-wackestones  
499 and open lagoon wackestones, occasional windward and leeward shoals of bioclastic pack-and-  
500 grainstones (34). The PTB and Early Triassic are regionally represented by ooidal grainstones  
501 and a thrombolite horizon (14, 34). Samples were taken from two transects Wadi Shahha (WSA)  
502 and Sha (SHA1), ~1000 m apart.. Facies are laterally continuous and carbon isotopes were used  
503 to ensure careful integration of the two datasets. For this study, we have analyzed 25 carbonate  
504 samples in total, taken in approximately 1 to 10 m scale intervals and covering a total thickness  
505 of 98 m, starting in the mid-Changhsingian (Permian), going up into the mid-Griesbachian  
506 (Triassic) and bracketing the complete Permian Triassic Boundary (PTB) extinction event (Table  
507 S1).

Table S1: Boron, carbon and oxygen isotope data from Wadi Bih; U.A.E.; pH values are derived from a simplified and non-dynamic calculation using the  $\delta^{11}\text{B}_{\text{SW}}$  range given by the model calculation and a constant  $\text{pK}_B$  for 25°C, 35 psu, 0 dbar.

Sample	Height (m)	Lithology	Age (Ma)*	$\delta^{13}\text{C}$ (‰)	$\delta^{18}\text{O}$ (‰)	$\delta^{11}\text{B}$ (‰) <sup>+</sup>	$2\sigma$ (‰) <sup>#</sup>	pH $\delta^{11}\text{B}_{\text{SW}}$ 34‰	pH $\delta^{11}\text{B}_{\text{SW}}$ 36.8‰
Wadi Bih (25° 50' 31.2"N 56° 06' 41.7"E)									
WSA54	14.0	micritic mudstone	252.13	4.20	-2.40	9.7(3)	0.7	7.7	6.7
WSA49	24.0	micritic mudstone	252.09	4.60	-0.50	11.8(3)	0.7	8.0	7.6
SHA1 1	32.4	dolograinstone	252.06	4.23	-3.19	11.4(2)	0.6	7.9	7.5
SHA1 3	37.0	grainstone	252.05	4.22	-2.62	10.8(0)	0.6	7.9	7.4
SHA1 4	39.0	micritic mudstone	252.04	4.26	-2.51	15.3(6)	0.8	8.3	8.1
SHA1 7	43.8	bioclastic packstone	252.02	3.63	-2.65	15.1(7)	1.0	8.3	8.0
SHA1 8	47.0	bioclastic packstone	252.01			13.7(12)	1.4	8.2	7.9
WSA22a	50.0	micritic mudstone	252.00	3.80	-3.50	13.8(5)	0.8	8.2	7.9
SHA1 11	51.0	bioturbated mudston	251.98			15.9(7)	0.9	8.3	8.1
WSA21	52.0	micritic mudstone	251.97	2.10	-4.00	15.7(2)	0.6	8.3	8.1
WSA 17	55.0	micritic mudstone	251.95	2.54	-3.65	15.3(2)	0.6	8.3	8.1
SHA1 15	59.6	calcsphere grainston	251.92	0.52	-3.15	15.8(21)	2.2	8.3	8.1
SHA1 17	62.0	calcsphere grainston	251.90			13.1(12)	1.4	8.1	7.8
WSA12A	64.0	micritic mudstone	251.90	0.50	-3.40	13.3(0)	0.6	8.1	7.8
SHA1 20	66.0	calcsphere grainston	251.90			15.0(13)	1.5	8.3	8.0
WSA5A	77.0	micritic mudstone	251.89	1.50	-3.20	12.9(0)	0.6	8.1	7.8
SHA1 26	78.2	calcsphere grainston	251.89	1.21	-2.55	13.6(10)	1.2	8.2	7.9
WSA3	85.0	micritic mudstone	251.88	1.60	-2.60	12.0(12)	1.3	8.0	7.6
SHA1 30	86.2	calcsphere grainston	251.88			12.5(6)	0.6	8.1	7.7
WSA 2A	86.8	micritic mudstone	251.88	1.99	-2.96	8.2(10)	1.2	7.4	-
WSA2	88.0	micritic mudstone	251.88	1.60	-2.94	8.6(18)	1.9	7.5	<7.0
WSA 1B	89.0	micritic mudstone	251.88	1.87	-3.26	10.1(2)	0.6	7.8	7.0
SHA1 32	90.2	calcsphere grainston	251.88	1.39	-3.40	11.6(8)	1.0	8.0	7.6
WSA1	91.0	micritic mudstone	251.88	1.46	-3.74	14.8(0)	0.6	8.2	8.0
SHA1 36	102.0	bioclastic packstone	251.86	1.79	-2.00	13.3(17)	1.8	8.1	7.8

\* Ages are calculated based on tie points from Burgess et al.(2), see section S1.2

<sup>+</sup> external uncertainty for B isotope data are valid for the last digits (2 $\sigma$ )

<sup>#</sup> propagated uncertainties for B isotope data

## 1.2 Age Model

The age model for this study was based on the most recent findings of Burgess et al., (2) (see Table S1). The age tie points are 252.10 Ma for 20 m (Fig. 2) thought to be equivalent to Bed 22 in Meishan from the  $\delta^{13}\text{C}$  record; 252.00 Ma for the decline in  $\delta^{13}\text{C}$  at 49 m and 251.90 Ma for the first occurrence of *H. parvus* at 61m. EP2 is known to occur at the end of the *I. staeschi* zone, Bed 28 Meishan (3), which is not recorded in the Neo-Tethys but is equivalent to the carbon

isotope rise between the *H. Parvus* and *I. isarcica* zones. In Wadi Bih we see the loss of gastropods and bivalves at this point (34), however the full resolution of the second extinction phase has not been confirmed at this locality. Therefore we identify a 10 m interval for EP2. In order to complete the age model we set the mid-point of EP2 as 251.88 Ma based on the absolute age for EP2 in Meishan (2).

### 1.3 Analytical methods

Carbon and oxygen isotope ratios were determined at Edinburgh University and University of Graz using the preparation technique and measurement routine as detailed in (19). All carbonate isotopic values are quoted in the conventional  $\delta$  per mil (‰) notation relative to VPDB. Calibration to international reference material was through NBS 19 and the reproducibility of replicate analyses for reference material, standards (in-house) and carbonate samples was better than  $\pm 0.05$  ‰ for  $\delta^{13}\text{C}$  and  $\pm 0.1$  ‰ for  $\delta^{18}\text{O}$  at one standard deviation. For a detailed discussion of the C and O isotopic data see (19).

Boron isotope ratios were determined in the isotope geochemistry laboratory at the University of Bremen (Department of Geosciences and MARUM-Center for Marine Environmental Sciences) using a ThermoFisher Scientific TRITON Plus Thermal Ionization Mass Spectrometer. The  $n(^{11}\text{B})/n(^{10}\text{B})$  measurements were performed using negative thermal ionization mass spectrometry (N-TIMS) following the method detailed in (37). For analyses, 10 mg of the sample powder was dissolved in 100  $\mu\text{l}$  1 N HCl for 24 h at 20°C and subsequently centrifuged. 1  $\mu\text{l}$  boron-free seawater emitter (38) together with 1  $\mu\text{l}$  of the sample solution containing  $\sim 1$  ng B were placed and dried on a degassed Re single filament. Analyses were carried out at filament temperatures of 970°-1050°C. Boron isotopes were registered as  $\text{BO}_2^-$

complexes on masses 42 and 43, and measurements were carried out at ion beam intensity of ~ 10 pA on mass 43. Each sample measurement involved up to 200 blocks with 10 cycles each, taking about 2 hours of data acquisition. B isotope ratios are given relative to NIST SRM 951 in the conventional  $\delta^{11}\text{B}$  (‰) notation. The external reproducibility of the certified reference material NIST SRM 951 showed an  $n(^{11}\text{B})/n(^{10}\text{B})$  ratio of  $4.0065 \pm 0.0017$  ( $2\sigma = 0.42\text{‰}$ ,  $n=23$ ) over a period of 6 month of sample analyses. The long term (18 month) reproducibility is  $4.0066 \pm 0.0018$  ( $2\sigma = 0.44\text{‰}$ ,  $n=58$ ). The  $n(^{11}\text{B})/n(^{10}\text{B})$  ratio of the reference material for each analytical session was reproduced better than  $0.6\text{‰}$  ( $2\sigma$ ). In addition to the NIST material, the standard material M93-TB-FC-1, a *Porites* coral with a published value of  $24.8 \pm 0.4\text{‰}$  ( $2\sigma_{\text{mean}}$ ), as determined by different multicollector techniques (39) was also regularly analysed. The coral replicates gave  $\delta^{11}\text{B}$  values of  $24.1 \pm 0.7\text{‰}$  ( $2\sigma$ ,  $n=16$ ). Each sample solution was as a minimum run in full duplicate and the uncertainty of the reference material was propagated into the external uncertainty ( $2\sigma$ ) on the isotope ratio of the sample ( $2\sigma_f$ ; Table S1). For further information on the preparation and analytical methods see (40).

## 2. Sample Selection

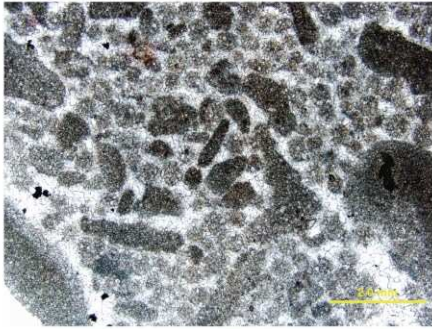
A critical issue in using the B isotope composition of Permo-Triassic carbonate rocks for reconstruction of ocean pH is the potential overprinting of the original isotope signal via alteration. To obtain high-quality samples in which primary B isotope signals are still preserved, we applied the sample selection procedures successfully used on Neoproterozoic carbonate rocks to reconstruct Cryogenian and Ediacaran ocean pH variation (37, 40, 41). In brief, samples selected for isotope analyses were screened macroscopic (in the field), microscopic (scanning electron microscope) and geochemically (carbon and oxygen isotopes), and selected because of

their uniformity in texture, absence of late stage secondary alteration and no correlation between carbon and boron with oxygen isotopic signatures (Figs. S1 and S2).

The PTB interval itself was thought to occur in a regional cross-bedded ooid grainstone, however, reconsideration of published thin-section images (34) (Fig S1 samples from WSA transect, 0611300847 and 0611181243) demonstrate these are in fact microspheres (a.k.a calcispheres). This fabric is unusual for the Phanerozoic but appears to represent supersaturated conditions and these are thought to be primary spar precipitates (42).

To gain the highest potential for recording a primary boron signature we microdrilled areas of pure micrite from micritic mudstones and micritised calcisphere grainstones where there was no micro-optical evidence for veining, fracturing, clay minerals or bioclastic material. Samples containing evidence of late stage secondary alteration or recrystallization, i.e. any spar/microspar, were discarded. Potential analyses of disseminated detrital material in the carbonates was also checked through elevated Al, Si and Ba concentrations and showed either no or only minor dissemination of clay. The low availability of bioclastic material in this interval, due to the extinction, argues against the potential of trends being caused by vital effects. In particular the calcisphere grainstones of the PTB interval are classed as an abiotic carbonate that provides an excellent opportunity to record seawater  $\delta^{11}\text{B}$  in the absence of vital effects.

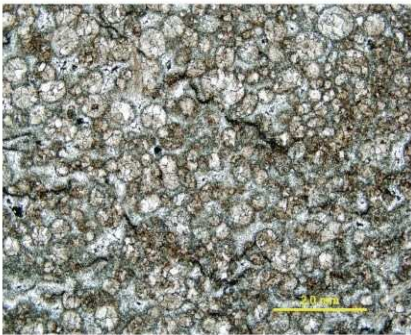
0611301104 (87m)



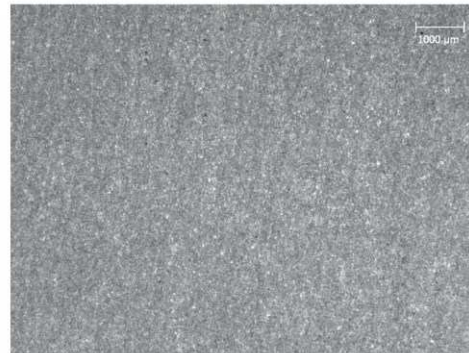
WSA1 (91m)



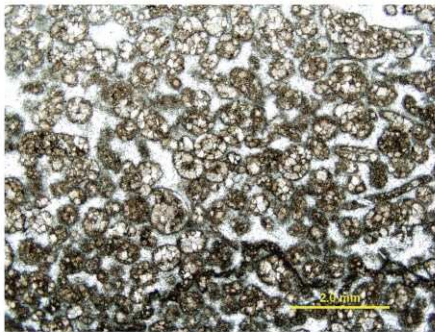
0611300847 (77m)



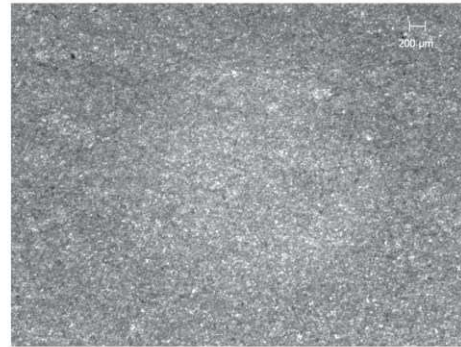
WSA2 (86m)



0611181243 (56m)



WSA3 (85m)



580

581 Fig S1: Examples of thin section images for the Wadi Bih section, WSA transect. WSA samples  
582 demonstrate homogeneous micritic texture of samples used for  $\delta^{11}\text{B}$  analysis. 06- samples are from  
583 Maurer et al., (34) illustrating grainstones. The lack of compaction of grains and pore filling equant  
584 spar cements indicate very early/syn-sedimentary cementation. This fabric is consistent with  
585 indicators for supersaturated conditions in this interval, including thrombolites and flat pebble  
586 conglomerates, and suggests preservation of the original depositional fabric. Sample heights (m) as  
587 in Fig. 2 and Table S1.

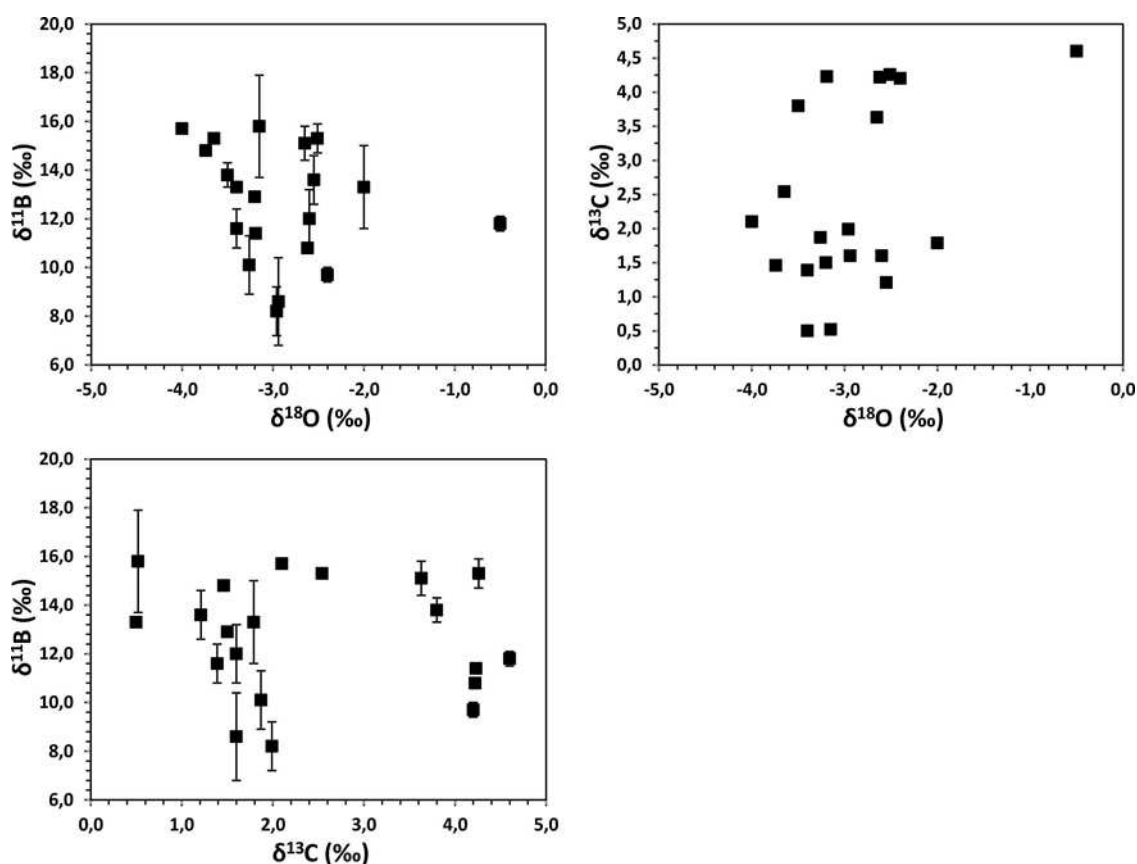


Fig S2: Cross-plots of boron, carbon, and oxygen isotope data for the marine carbonate samples from the Wadi Bih section. No significant correlation can be observed.

## 2.1 Diagenetic Influences

The PTB interval grainstone is composed of microspheres (a.k.a calcispheres). Microspheres are micritized and cemented with coarse equant spar cement (Fig S1). The lack of compaction of the microspheres suggests that the spar cement was extremely early and probably syn-sedimentary. This is a feature of other grainstones throughout this interval (WSA transect, sample 0611301104). Critically the presence of such well cemented fabrics in the grainstones of this interval would have prevented later stage fluid migration, and hence any late stage dolomitization. The total negative boron isotope excursion at EP2 is recorded across a number of fabrics and facies, including micrite and the early cemented grainstones. Petrographic analysis

shows the extreme of the acidification event is recorded in fine-grained micrite where textures are very homogenous samples WSA 1, 1B, 2, and 2A (Fig. S1).

Dolomitization in the Wadi Bih section is observed (14), and occurred in two phases where the first phase was fabric retentive syn-sedimentary dolomitization. The second phase of dolomitization leads to the recrystallization of facies where near depositional porosity and permeability had been maintained, i.e. preferentially in non-cemented grainstones. Neither of these phases is classed as deep burial dolomitization (as confirmed by petrography in Figure S1 and the  $\delta^{18}\text{O}$  data, Table S1). In the Musandam Peninsula the impact of dolomitization on carbon and oxygen isotopes can be seen only in the close proximity to regional faults that provided high permeability pathways for late burial dolomitizing fluids (43), which were avoided for this study.

Diagenetic effects were also checked with geochemical tests for selected trace element analyses, using secondary ionisation mass spectrometer Cameca ims 4f at the University of Edinburgh. Diagenetic alteration was explored via Mn/Sr, which is often used as a geochemical indicator of alteration and meteoric diagenesis in ancient carbonates (44). While low Mn/Sr has been found in ancient carbonates where there is clear optical evidence for recrystallization (45), high Mn/Sr may indicate carbonate precipitation from anoxic waters. In the selected samples, Mn concentration is  $< 300 \mu\text{g g}^{-1}$ , Sr concentration ranges from 140 to 1400  $\mu\text{g g}^{-1}$ , and the Mn/Sr ratio is low ( $< 2$ ), so suggesting no influence of meteoric fluids. The boron concentration for the carbonate rocks is, on average,  $1 \mu\text{g g}^{-1}$  and ranges between 0.2 and  $1.7 \mu\text{g g}^{-1}$ .

Post-depositional alteration, especially meteoric diagenesis and recrystallization, is assumed to decrease the isotopic composition of oxygen, boron and carbon isotopes (e.g. 46-48). Our selected carbonate samples show the distinct carbon isotope trend found at every PTB section globally and  $\delta^{18}\text{O}$  values ranging between -0.5 and -4.0‰, indicating no significant deep

burial alteration. All carbon and oxygen isotope data are given in Table S1. No statistically significant correlation between carbon, oxygen and boron isotope data can be observed in our data (Fig. S2).

The replication of the  $\delta^{11}\text{B}$  across two complementary transects further support the preservation of a primary seawater isotope signature as late stage dolomitization is expected to be highly laterally variable and disrupt the smooth trends seen in the data.

### **3. Support for a primary Boron isotope signature**

#### ***3.1 Published $\delta^{11}\text{B}$ data***

So far,  $\delta^{11}\text{B}$  data for Triassic carbonates have not been published and only limited  $\delta^{11}\text{B}$  data, based on low-Mg calcite brachiopod calcite from Oman (Saiwan Fm.), are available for the Permian (Late Sakmarian). Keeping in mind the modern residence time of boron ( $T \sim 14$  to  $20$  Ma (47, 49), it is important to note that the range in  $\delta^{11}\text{B}$  values ( $10.9 \pm 0.9\text{‰}$  ( $1\sigma$ ,  $n=4$ ), 252.05-252.15 Ma, mid-Changhsingian) overlap with the range in  $\delta^{11}\text{B}$  values between 10.1 and 11.7‰ of the 285 Ma old brachiopod carbonates (average  $10.6 \pm 0.\text{‰}$ ,  $1\sigma$ ,  $n=5$ , (16)), which support the primary nature of our boron isotope data.

#### ***3.2 Environmental controls on the boron isotope composition***

The speciation of boron in seawater is predominantly pH dependent with minor controls from temperature, salinity and pressure (50). In our model we consider a dynamic temperature effect on  $pK_B$  to calculate the pH of the seawater from the boron isotope composition preserved in Permo-Triassic carbonate (see SM 4 and 5) however below we evaluate geological evidence to consider whether these variables could drive the trends seen in our data.

### 3.2.1 Temperature

Oxygen isotope data preserved in conodont apatite and low-Mg calcite brachiopods from Permian-Triassic sections in Iran document tropical sea surface temperatures (SST) of 27–33°C during the Changhsingian with a negative shift in  $\delta^{18}\text{O}$  starting at the extinction horizon, translating into a warming of SSTs to well over 35°C in the mid-Griesbachian (51). The results are consistent with SSTs of the South Chinese sections, where a rapid increase in seawater temperature from about 25° to 36°C across the Permian-Triassic section was proposed based on conodont apatite (6). Since the dissociation constant of boric acid ( $pK_B$ ) decreases with increasing temperature (50), the proposed increase in SST could drive an increase in the B isotope composition of the carbonates precipitated at the time of global warming and imply an increase in ocean pH, even if ocean pH stayed stable. Using the  $pK_B$  data from (50), the potential increase in SST at a given pH of 8 would drive an increase in  $\delta^{11}\text{B}$  of the carbonates by 2‰ and generate an artificial increase of < 0.2 pH units. Consequently, it could be argued that our calculated pH variations are in essence the result of an increase in sea surface temperatures. However, the oxygen isotope pattern (51) shows a continuous increase in temperatures across the Permian-Triassic boundary and a thermal maximum in the mid-Griesbachian (~251.85 Ma). Instead our data show a sharp increase in  $\delta^{11}\text{B}$  and ocean pH in the Late Permian, well before the increase in temperatures at EP1. The slight variability in  $\delta^{11}\text{B}$  above the PTB, however, could be driven by temperature variations.

### 3.2.2 Salinity

Similar to temperature, the  $pK_B$  is sensitive to salinity and increases with decreasing salinity (52). To drive significant salinity-associated isotope variations across the Permo-Triassic boundary, drastic changes in salinity (e.g. down to 25 psu compared to 35 psu) would be necessary. However, even if modelled sea surface salinity values for the late Permian indicate generally more saline conditions than present day (52), sea surface salinity values for e.g. Iran and South China still range between 34 and 35 psu (51) and will not have a significant effect on our pH calculation. These samples come from an exclusively shallow water environment far from any freshwater input, and so decreases in salinity would not affect our pH interpretations. The depositional environment here ranges between open water ooid shoals to open and restricted lagoon settings, which results in cyclic deposition on the scale of 5m. A shift toward more restricted settings could drive increases in salinity that would affect the  $\delta^{11}\text{B}$  record; however, these depositional cycles are not on the same scale as the secular trends seen in  $\delta^{11}\text{B}$ .

### 3.2.3 Water Depth

Permo-Triassic seawater pH values have been reconstructed assuming carbonate precipitation at sea surface conditions. Modern bathymetric pH and temperature profiles from the tropics show that pH can decrease by up to ~0.2 units and temperature can drop by 15°C in the first 300 m (53). Thus the B isotope composition of carbonates precipitated at greater water depths would be more negative compared to surface precipitates. This potential depth effect is thought to be of minimal influence to the Wadi Bih carbonates due to the exclusively shallow marine (subtidal to intertidal) nature of the succession.

Consequently, uncertainties in the  $\delta^{11}\text{B}$ -ocean pH relationship potentially introduced by changes in temperature, salinity, bathymetry or biofacies would not be able to produce the observed B isotope pattern with the sharp increase in the mid-Changhsingian (~252.04 Ma) and the temporary decrease in the mid-Griesbachian (~251.88 Ma), but would be capable of explaining some of the slight variations across the PTB.

#### 4. Boron-pH calculations

The boron isotope composition of marine carbonates is used to reconstruct seawater pH values and atmospheric  $\text{pCO}_2$  concentrations (e.g. 54-58). The application of the B isotope system as a proxy for ocean pH is based on the observation that the fractionation factor for isotope exchange between the two different speciation of boron ( $\text{B(OH)}_3$  and  $\text{B(OH)}_4^-$ ) is pH sensitive and produces significant and traceable changes in the isotopic composition of carbonates (e.g. 57).

The carbonate-associated boron isotopic composition  $\delta^{11}\text{B}_{\text{carb}}$  is assumed to be equal to that of seawater  $\text{B(OH)}_4^-$ . The isotopic composition of the two boron species  $\text{B(OH)}_4^-$  and  $\text{B(OH)}_3$  is determined by the isotopic fractionation factor  $\alpha_{\text{B3-B4}} = 1.0272$  (59), the speciation (a strong function of pH, with smaller dependencies on temperature, pressure and salinity), and the overall isotopic composition of seawater  $\delta^{11}\text{B}_{\text{sw}}$ . The relationship between pH and  $\delta^{11}\text{B}_{\text{carb}}$  is given by:

$$\text{pH} = \text{pK}_B - \log \left[ - \frac{\delta^{11}\text{B}_{\text{sw}} - \delta^{11}\text{B}_{\text{carb}}}{\delta^{11}\text{B}_{\text{sw}} - \alpha_{\text{B3-B4}} \cdot \delta^{11}\text{B}_{\text{carb}} - 1000 \cdot (\alpha_{\text{B3-B4}} - 1)} \right]$$

where the effective dissociation constant  $\text{pK}_B$  includes the temperature, pressure and salinity dependence. We dynamically calculate  $\text{pK}_B$  using CO2SYS-MATLAB v1.1 (60) (detailed in SM 5), which is consistent with the calculation and constants used by (61).

A prerequisite for reconstruction of past ocean pH values via B isotope data is the knowledge of the primary B isotope composition  $\delta^{11}\text{B}_{\text{SW}}$  of the ambient seawater. The B isotope composition of modern seawater is regarded as being homogeneous with a  $\delta^{11}\text{B}$  value of 39.5‰ (54). However, recent work on Precambrian to Phanerozoic carbonates and evaporites has shown that the B isotope composition of seawater was highly variable in the geological past (16, 45, 46) driven mainly by variations in the global boron budget during Earth history (23), exceeding the residence time of B in seawater. Permo-Triassic seawater have been calculated based on changes in processes controlling the oceanic boron budget, e.g. oceanic crust production rate and continental boron flux (16) and suggests  $\delta^{11}\text{B}_{\text{SW}}$  values of ~38‰ for the early Permian (285 Ma, Late Sakmarian) and ~34‰ just before the PTB (16).

Given this uncertainty in  $\delta^{11}\text{B}_{\text{SW}}$ , we consider a range of values, determined by the overall consistency of the  $\delta^{11}\text{B}_{\text{carb}}$  data with model-derived constraints on the seawater carbonate chemistry and hence pH, resulting in an envelope for the pH calculation. The model scenarios encompass the range of previous estimates for background Early Permian conditions (13), which suggest either high  $p\text{CO}_2$  with lower pH ( $\text{CO}_2\text{Hi}$ : ~10 PAL, pH ~7.5), or low  $p\text{CO}_2$  with higher pH ( $\text{CO}_2\text{Lo}$ : ~3 PAL, pH ~8). In our model we consider these two scenarios with corresponding seawater boron isotopic composition ( $\delta^{11}\text{B}_{\text{SW}} = 34\text{‰}$  and  $36.8\text{‰}$ ) required to reproduce the observed  $\delta^{11}\text{B}_{\text{carb}}$  (see SM Section 6 for further details of the model scenarios).

We illustrate the effect of uncertainties in  $\delta^{11}\text{B}_{\text{SW}}$  and temperature on pH, and the overall consistency with the  $\delta^{11}\text{B}_{\text{carb}}$  data in Figure S3 and Table S1 (note that the full model described in SM 4 also includes a dynamic calculation of temperature). The lowest  $\delta^{11}\text{B}_{\text{SW}} = 34\text{‰}$  and highest pH considered (scenario  $\text{CO}_2\text{Lo}$ ) is effectively constrained by the model limitation on the highest pH values immediately prior to EP1. The highest  $\delta^{11}\text{B}_{\text{SW}} = 36.8\text{‰}$  and lowest pH

(scenario  $\text{CO}_2\text{Hi}$ ) is effectively constrained by the limit of propagated uncertainty ( $2\sigma$ ) on the lowest observed  $\delta^{11}\text{B}_{\text{carb}}$  combined with the non-linearity of the B isotope system.

An additional uncertainty in interpreting  $\delta^{11}\text{B}_{\text{carb}}$  is introduced by any potential offset or fractionation between seawater borate  $\delta^{11}\text{B}(\text{OH})_4^-$  and  $\delta^{11}\text{B}_{\text{carb}}$ . As shown by (59), the laboratory measured fractionation of abiotic carbonate (61) shows both an offset relative to that of the artificial seawater, and a shallower slope with increasing pH. As we consider  $\delta^{11}\text{B}_{\text{SW}}$  as a model parameter to be determined, an overall offset is effectively subsumed within this. However a shallower slope than that used here ( $^{11-10}\text{K}_\text{B} = 1.0272$  [ref 59], cf the one given for inorganic carbonates (1.0267; [ref 62])) would require a larger pH change for a given observed change in  $\delta^{11}\text{B}_{\text{carb}}$ . Sanyal et al. (63) published B isotope values for inorganic calcite precipitates at three different pH conditions - 7.9, 8.3, and 8.6. This same experimental inorganic calcite data and associated estimates of  $^{11-10}\text{K}_\text{B}$  in seawater were also presented by Klochko et al. (59, 64). To date, there is no agreement as to the actual deviation of Sanyal's data (63) from the now generally-accepted empirical fractionation factor given by Klochko et al (59). A best fit value of 1.0267 for the inorganic calcite precipitation was given by Pagani et al. (62). But by contrast, the deviation between the inorganic carbonate values and the empirical fractionation appears much bigger in Klochko et al. (59) and the best-fit value is given as 1.0260. This increased deviation is explained by the difference in pH scale between natural or artificial seawater used for the calibration experiments, and the experimental seawater pH measured on the (freshwater) NBS scale. Klochko et al. (64) tries to address the deviations in  $\delta^{11}\text{B}$  of inorganic precipitates from empirical calibration studies and concludes that boric acid incorporation may contribute to the  $^{11}\text{B}$  enrichment observed in inorganic precipitates, especially at lower pH. They point out,

however, that all carbonates precipitated under controlled pH conditions were enriched in  $^{11}\text{B}$  relative to seawater borate (63).

If we use the best fit value (1.0267) given by Pagani et al. (62) for the inorganic carbonates (Sanyal et al 2000) instead of the empirical value of Klochko et al. (59), then the offset for the majority of the data would be around 0.05 pH units. Visible changes to more acidic values would only appear at the lowermost pH estimates, but would still be less than 0.2 pH units and fall within the general uncertainty. If we take the 1.026 value, the offset would generally increase between  $\leq 0.1$  and 0.2 (pH range between  $\sim 8.4$  and 7.8) but would indeed result in significantly lower pH values of up to 0.5 units for the acidification event.

Given the limited amount of experimental inorganic calcite data and this disagreement between the best-fit values, we have taken the simplest approach for the model representation and chosen to use the most generally-accepted empirical fraction factor given by Klochko et al. (59).

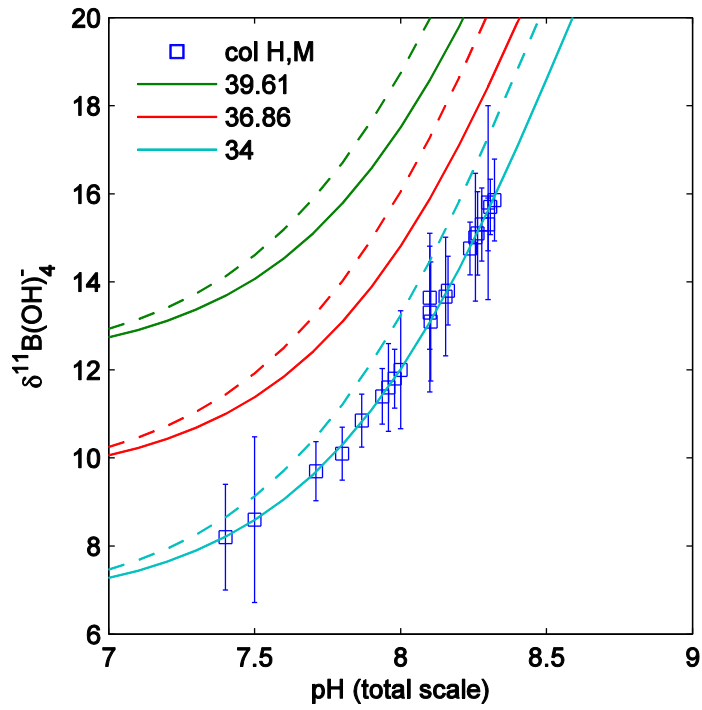


**Figure S3** Effect of background  $\delta^{11}\text{B}_{\text{SW}}$  and temperature on relationship between  $\delta^{11}\text{B}_{\text{carb}}$  and pH (total scale), for conditions appropriate to low-latitude surface ocean (atmospheric pressure, salinity 35 psu, temperature 25°C (solid lines) and 35°C (dashed lines)). Three values are shown for  $\delta^{11}\text{B}_{\text{SW}}$ : 39.61‰ (the contemporary value) and two values consistent with the end Permian data. Data points and  $2\sigma$  errors are overlaid for the  $\delta^{11}\text{B}_{\text{SW}}$  34‰ case.

## 5. Model Description

### 5.1 Overview

The overall model structure (shown in Figure S4) is essentially a superset of carbon cycle models previously applied to the end Permian (65, 66, 67), with additional consideration of the marine sulphur cycle. The model includes a three box ocean model as the minimum needed to demonstrate the effect of the biological pump on vertical DIC gradients and ocean redox state. The model is implemented as a set of coupled differential equations for the time evolution of reservoirs (Table S3), exchanging fluxes according to air-sea exchange, ocean circulation, applied external forcings and perturbations, and the biogeochemical processes described in Table S5. Model constants are defined in Table S4. The model implements an open inorganic carbon cycle, with atmospheric  $p\text{CO}_2$  and marine DIC and Alk determined by the feedbacks between land-surface carbonate and silicate weathering and marine carbonate deposition. Oxidative weathering, volcanic degassing, and land and marine organic carbon burial are specified as forcings, as is marine phosphorus and hence productivity.

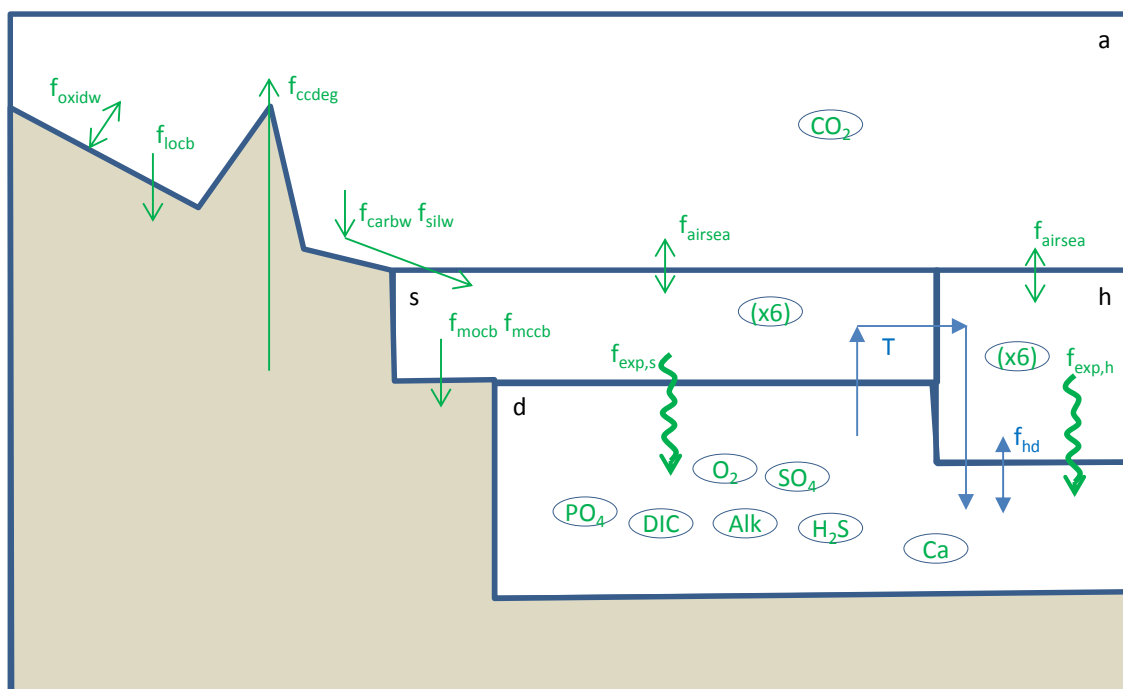


Figure S4 Model schematic. Ocean is represented by three boxes (s, h, d), with well-mixed atmosphere box a. Biogeochemical fluxes are shown in green, ocean circulation in blue. Biogeochemical reservoirs are shown as ovals.

Table S3 Model reservoirs

Reservoir	Initial size	Description
<b>Atmosphere</b>		
$\text{CO}_2$	eqb <sup>a</sup>	Atmospheric $\text{CO}_2$
<b>Ocean</b>		
$\text{DIC}_{(s,h,d)}$	eqb <sup>a</sup>	Total carbon
$\text{Alk}_{(s,h,d)}$	eqb <sup>a</sup>	Total alkalinity
$\text{O}_{2(s,h,d)}$	eqb <sup>a</sup>	Oxygen
$\text{PO}_{4(s,h,d)}$	2.15 $\mu\text{M}$ / kg-sw	Phosphate
$\text{SO}_{4(s,h,d)}$	28 mM / kg-sw	Sulphate
$\text{H}_2\text{S}_{(s,h,d)}$	0	Sulphide
Ca	10.28 mM / kg-sw	Calcium (single reservoir)

<sup>a</sup> set by initial spin-up to steady-state.

Table S4 Model fluxes, constants, and forcings.

Flux	Model Parameter	Value	Units	Description
<b>crust/mantle</b>				
$f_{\text{ccdeg}}$	$k_{12\_ccdeg}$	varies <sup>a</sup>	mol CO <sub>2</sub> yr <sup>-1</sup>	Degassing
<b>land surface</b>				
$f_{\text{carbw}}$	$k_{14\_carbw}$	1.33x10 <sup>13</sup>	mol CaCO <sub>3</sub> yr <sup>-1</sup>	Carbonate weatherability
$f_{\text{silw}}$	$k_{\text{silw}}$	varies <sup>a</sup>	mol "CaSiO <sub>3</sub> " yr <sup>-1</sup>	Silicate weatherability
$f_{\text{oxidw}}$	$k_{17\_oxidw}$	varies <sup>a</sup>	mol C yr <sup>-1</sup>	Oxidative weathering
$f_{\text{locb}}$	$k_{5\_locb}$	5x10 <sup>12</sup>	mol C yr <sup>-1</sup>	Land organic carbon burial
<b>marine</b>				
	$k_{O\_Asurf(s)}$	0.85x3.6	m <sup>2</sup>	Ocean surface area
	$k_{O\_Asurf(h)}$	x10 <sup>14</sup>		
		0.15x3.6	m <sup>3</sup>	Ocean volume
		x10 <sup>14</sup>		
	$k_{O\_vol(s)}$	3.06 x10 <sup>16</sup>		
	$k_{O\_vol(h)}$	1.35 x10 <sup>16</sup>		
	$k_{O\_vol(d)}$	1.60 x10 <sup>21</sup>	Sv	Overturning circulation
T	$k_{O\_circT}$	20		
$f_{\text{hd}}$	$k_{O\_circfhd}$	60	Sv	High latitude – deep exchange
	$k_{\text{piston}}$	0.3	m d <sup>-1</sup>	Air-sea piston velocity
	$T_{O(s)}$	$T_{\text{mean}} + 6.5$		Ocean temperature
	$T_{O(d)}$	$\max(T_{\text{mean}} - 12.5, 2.5)$		
	$k_{O\_sal}$	35	psu	Ocean salinity
	$r_{c:p}$	161		Redfield C:P ratio
	$r_{n:p}$	16		Redfield N:P ratio
$f_{\text{mccb}}$	$k_{\text{carbsedshallow}}$	varies <sup>a</sup>	mol CaCO <sub>3</sub> yr <sup>-1</sup>	Marine carbonate burial
$f_{\text{mocb}}$	$k_{2\_mocb}$	5x10 <sup>12</sup>	mol C yr <sup>-1</sup>	Marine organic carbon burial

<sup>a</sup> parameters  $k_{\text{silw}}$ ,  $k_{12\_ccdeg}$ ,  $k_{\text{carbsedshallow}}$  are per-scenario external forcings.

Table S5 Biogeochemical processes

Flux	Biogeochemical transformation	Stoichiometry							Rate		Description
		CO <sub>2(a)</sub>	DIC	Ca	O <sub>2</sub>	P	H <sub>2</sub> S	SO <sub>4</sub> <sup>2-</sup>	Alk		
land surface											
f <sub>carbW</sub>	CO <sub>2</sub> + H <sub>2</sub> O + CaCO <sub>3</sub> → Ca <sup>2+</sup> + 2HCO <sub>3</sub> <sup>-</sup>	-1	2	1					2	Equation (S2)	Carbonate weathering
f <sub>silw</sub>	2CO <sub>2</sub> + H <sub>2</sub> O + CaSiO <sub>3</sub> → SiO <sub>2</sub> + Ca <sup>2+</sup> + 2HCO <sub>3</sub> <sup>-</sup>	-2	2	1					2	Equation (S1)	Silicate weathering
f <sub>oxidw</sub>	CH <sub>2</sub> O + O <sub>2</sub> → CO <sub>2</sub> + H <sub>2</sub> O	1	0	0					0	k <sub>17_oxidw</sub>	Oxidative weathering
f <sub>locb</sub>	CO <sub>2</sub> + H <sub>2</sub> O → CH <sub>2</sub> O + O <sub>2</sub>	-1	0	0					0	k <sub>5_locb</sub>	Organic carbon burial
marine											
f <sub>exp</sub>	CO <sub>2</sub> + H <sub>2</sub> O + xP → CH <sub>2</sub> OP <sub>x</sub> + O <sub>2</sub>	-1	0	0	1+	-1/r <sub>cp</sub>	0	0	r <sub>np</sub> /r <sub>cp</sub> <sup>a</sup>	see Section 3.2.4	Export production
	CH <sub>2</sub> OP <sub>x</sub> + O <sub>2</sub> → CO <sub>2</sub> + H <sub>2</sub> O + xP	1	0	0	-1-	1/r <sub>cp</sub>	0	0	-r <sub>np</sub> /r <sub>cp</sub> <sup>a</sup>	see Section 3.2.4	Aerobic remineralisation
	CH <sub>2</sub> OP <sub>x</sub> + $\frac{1}{2}$ SO <sub>4</sub> <sup>2-</sup> → HCO <sub>3</sub> <sup>-</sup> + xP + $\frac{1}{2}$ H <sub>2</sub> S	1	0	0	0	1/r <sub>cp</sub>	0.5	-0.5	1	see Section 3.2.4	Sulphate reduction
	H <sub>2</sub> S + 2O <sub>2</sub> → SO <sub>4</sub> <sup>2-</sup> + 2H <sup>+</sup>	0	0	0	-2	0	-1	1	-2	see Section 3.2.4	Sulphide oxidation
f <sub>mccb</sub>	Ca <sup>2+</sup> + HCO <sub>3</sub> <sup>-</sup> → H <sup>+</sup> + CaCO <sub>3</sub>	-1	-1	-1	0	0	0	0	-2	k <sub>carbsedshallow</sub> x(Ω <sub>aragonite</sub> -1) <sup>1.7</sup>	Carbonate deposition
	2H <sub>2</sub> S + Fe(OH) <sub>3</sub> → FeS <sub>2</sub> + $\frac{1}{2}$ H <sub>2</sub> + 3H <sub>2</sub> O	0	0	0	-0.5	0	-2	0	0		Pyrite formation and burial
f <sub>mocb</sub>	CO <sub>2</sub> + H <sub>2</sub> O → CH <sub>2</sub> O + O <sub>2</sub>	-1	0	0	1	0	0	0	0	k <sub>2_mocb</sub>	Organic carbon burial

<sup>a</sup> contribution from nitrate, assumed at Redfield ratio.

## 5.2 Detailed description

### 5.2.1 $p\text{CO}_2$ and temperature

Global mean temperature  $T_{\text{mean}}$  is calculated from atmospheric  $p\text{CO}_2$  using the energy balance model as in COPSE (68, 69), with solar insolation appropriate for 250 Mya. Marine temperature  $T_{\text{O(s,h,d)}}$  is calculated from the global mean assuming a fixed high-low latitude temperature difference and minimum temperature of  $2.5^\circ\text{C}$ , with  $T_{\text{O(s)}}=T_{\text{mean}}+6.5^\circ\text{C}$  and  $T_{\text{O(h,d)}}=\max(T_{\text{mean}}-12.5, 2.5)^\circ\text{C}$ .

### 5.2.2 Land surface weathering, degassing, and organic carbon burial

Land surface weathering is essentially a stripped-down version of that in COPSE (69), with carbonate and silicate weathering included but sulphur weathering and the long-timescale sedimentary reservoirs for sulphur and carbon are omitted. Atmospheric oxygen is fixed at the present-day value. Silicate and carbonate weathering are controlled by atmospheric  $p\text{CO}_2$  and temperature with functional forms:

$$f_{\text{silw}}=k_{\text{silw}} e^{0.090(T_{\text{mean}}-T_0)} [1 + 0.038(T_{\text{mean}} - T_0)]^{0.65} \left( \frac{2 p\text{CO}_2}{1 + p\text{CO}_2} \right) \quad (\text{S1})$$

$$f_{\text{carbw}}=k_{14\_carbw} [1 + 0.087(T_{\text{mean}} - T_0)] \left( \frac{2 p\text{CO}_2}{1 + p\text{CO}_2} \right) \quad (\text{S2})$$

where  $T_0=15^\circ\text{C}$ .

Atmospheric  $\text{CO}_2$  is consumed, and carbon, alkalinity and calcium supplied to the ocean, according to the stoichiometry defined in Table S5. Volcanic degassing, oxidative weathering, and land organic carbon burial are prescribed as forcings.

### 5.2.3 Marine circulation and air-sea exchange

Marine circulation is defined by a thermohaline circulation  $T$ , and high-latitude – deep exchange  $f_{hd}$ . The marine box model includes  $P$ ,  $O$ ,  $DIC$ ,  $Alk$ ,  $SO_4$ ,  $H_2S$  as per-box prognostic variables, along with  $DIC$   $\delta^{13}C$ . Marine carbonate chemistry is calculated using a modified version of CO2SYS-MATLAB v1.1 (60), extended to include sulphide alkalinity using the constants tabulated by (70). Air-sea exchange of oxygen and  $CO_2$  assume a fixed piston velocity and temperature-dependent solubility.

### 5.2.4 Marine productivity and burial

Productivity and hence the biological pump are controlled by the marine phosphorus circulation. Biomass is produced in the surface ocean boxes, and exported and remineralized in the deep box according to the processes and stoichiometries defined in Table S5. Productivity in the ‘s’ box is specified to consume all phosphorus down to negligible concentration. Productivity in the ‘h’ box is specified to consume a fraction 0.18 of input phosphorus. Remineralization in the deep ocean box consumes oxygen down to a limiting concentration of  $1\mu M$  and thereafter reduces sulphate to sulphide.

Shallow-water carbonate deposition occurs in the ‘s’ box only and is controlled by aragonite saturation state and a parameter representing a combination of shelf area and calcification effectiveness, ie a ‘Neritic’ ocean without pelagic calcifiers (71), functional form  $k_{carbsedshallow} * (\Omega_{aragonite} - 1)^{1.7}$ . Ocean carbonate compensation is not included, on the basis this will be small for a ‘Neritan’ ocean.

Marine organic carbon burial from the ‘s’ box and pyrite burial from the ‘d’ box are imposed as forcings. Given the uncertainties in controls on phosphorus input over the end-Permian interval, the marine phosphorus cycle is semi-closed (i.e. weathering feedback on phosphorus input is not included), with imposed perturbations (forcings) to source/sink

balance (riverine input vs burial) applied as inputs to the ‘s’ box to control phosphorus concentration.

### 5.2.5 Carbon isotopes

Carbon isotopes are implemented with additional reservoirs for each of atmospheric CO<sub>2</sub> and marine DIC<sub>(s,h,d)</sub>. Air-sea exchange fractionates according to the temperature-dependent equilibrium and kinetic factors determined by Zhang et al. (72). Marine export production is at fixed fractionation relative to DIC, with  $\delta^{13}\text{C}_{\text{exp}(s,h)} = \delta^{13}\text{DIC}_{(s,h)} - 25\text{‰}$ .

Volcanic degassing, carbonate weathering, and oxidative weathering are assumed to add carbon at fixed fractionations of -4.9‰, 2.65‰, and -25‰ respectively. Atmospheric CO<sub>2</sub> consumed by silicate and carbonate weathering (and added to the ocean ‘s’ box as DIC) is fractionated relative to atmospheric CO<sub>2</sub> according to the freshwater fractionation of Zhang et al. (72).

Land and marine organic carbon burial is at fixed fractionation relative to atmospheric CO<sub>2</sub> and marine DIC, with  $\delta^{13}\text{C}_{\text{locb}} = \delta^{13}\text{CO}_2 - 19\text{‰}$  and  $\delta^{13}\text{C}_{\text{moch}} = \delta^{13}\text{DIC}_{(s)} - 25\text{‰}$ . Marine inorganic carbon burial is assumed to not fractionate relative to DIC<sub>(s)</sub>.

### 5.2.6 Boron isotopes

Carbonate-associated boron isotopic composition  $\delta^{11}\text{B}_{\text{carb}}$  is assumed to be equal to that of seawater B(OH)<sub>4</sub><sup>-</sup>. Speciation of B(OH)<sub>4</sub><sup>-</sup> and B(OH)<sub>3</sub> is calculated using CO2SYS-MATLAB v1.1 (60). Isotopic composition is then calculated from speciation  $x_{\text{bo4}} = [\text{B(OH)}_4^-]/[\text{B total}]$  and seawater  $\delta^{11}\text{B}_{\text{sw}}$  as

$$\delta^{11}\text{B}_{\text{carb}} = \frac{\delta^{11}\text{B}_{\text{sw}} - 1000(1 - x_{\text{bo4}})(\alpha_B - 1)}{\alpha_B - x_{\text{bo4}}(\alpha_B - 1)}$$

with the isotopic fractionation factor  $\alpha_B = 1.0272$ .

662

### 663 5.2.7 Model spinup and steady state

664 The model pCO<sub>2</sub> steady-state is defined by the imposed degassing rate, organic carbon burial  
 665 and oxidation, and silicate weathering parameterisations, where these together define a  
 666 unique value for the steady-state atmospheric pCO<sub>2</sub> and temperature where  $f_{\text{ccdeg}} + f_{\text{oxidw}} =$   
 667  $f_{\text{silw}} + f_{\text{locb}} + f_{\text{mocb}}$ . During spin-up, the ocean chemistry and hence atmosphere-ocean CO<sub>2</sub>  
 668 partitioning adjust (on the silicate weathering timescale of ~100kyr) to a steady-state, with  
 669 the aragonite saturation state adjusting such that carbonate burial balances inputs from  
 670 carbonate and silicate weathering.

671

### 672 5.2.8 Sensitivity to seawater composition

673 The Mg and Ca composition of end-Permian seawater (as determined from fluid inclusions)  
 674 is consistent with that of modern seawater ([Mg] = 53 mmol/kg, [Ca] = 10.3 mmol/kg), but  
 675 with large uncertainties (6). Sulphate concentration may have been much lower than modern  
 676 values (73, 74). We estimate the uncertainties in carbonate system chemistry following the  
 677 approach of (75). We estimate the effect on  $K_1$  and  $K_2$  from model results (74) as:

$$\frac{K_1^*}{K_1} = 1 + 0.155 \frac{\Delta[\text{Mg}^{2+}]}{[\text{Mg}^{2+}]_m} + 0.033 \frac{\Delta[\text{Ca}^{2+}]}{[\text{Ca}^{2+}]_m} - 0.019 \frac{\Delta[\text{SO}_4^{2-}]}{[\text{SO}_4^{2-}]_m}$$

$$\frac{K_2^*}{K_2} = 1 + 0.641 \frac{\Delta[\text{Mg}^{2+}]}{[\text{Mg}^{2+}]_m} + 0.071 \frac{\Delta[\text{Ca}^{2+}]}{[\text{Ca}^{2+}]_m} - 0.054 \frac{\Delta[\text{SO}_4^{2-}]}{[\text{SO}_4^{2-}]_m}$$

678 where subscript m refers to modern values and an asterix to end-Permian values. Taking  
 679 extremal values  $[\text{Mg}^{2+}]^*/[\text{Mg}]_m=0.5$ ,  $[\text{Ca}^{2+}]^*/[\text{Ca}]_m=2$ ,  $[\text{SO}_4^{2-}]^*/[\text{SO}_4^{2-}]_m=0.1$ , we have  
 680  $K_1^*/K_1=1-0.078+0.033+0.0171=0.972$  or  $\text{p}K_1^*=\text{p}K_1+0.012$  (or for  $[\text{Mg}^{2+}]$  alone,  
 681  $K_1^*/K_1=0.92$ ,  $\text{p}K_1^*=\text{p}K_1+0.035$ ). For a fixed pCO<sub>2</sub>, this implies a corresponding decrease in  
 682  $[\text{HCO}_3^-]$  and hence DIC inventory, or equivalently an increase in pH for the same DIC  
 683 content. The corresponding effect on  $K_2$  is much larger,  $K_2^*/K_2=1-$

0.32+0.0171+0.049=0.75. We estimate the effect of Mg concentration on the calcite solubility constant  $K_{sp}$  using the parameterisation given by (76) as:

$$\frac{K_{sp}^*}{K_{sp,m}} = 1 - 0.0833 \left( \frac{[Mg^{2+}]_m}{[Ca^{2+}]_m} - \frac{[Mg^{2+}]^*}{[Ca^{2+}]^*} \right)$$

which gives  $K_{sp}^*/K_{sp}=1-0.33$ .

This sensitivity study shows that the uncertainty in  $K_1$  therefore introduces only a small uncertainty in pH ( $\sim < 0.03$ ) or equivalently a  $\sim 10\%$  uncertainty in DIC inventory relative to  $pCO_2$ . The combined uncertainties in  $K_2$ ,  $K_{sp}$  and  $[Ca^{2+}]$  are larger, introducing corresponding uncertainties in calcite saturation state. However, within the model employed here, this is effectively absorbed into a rescaling of the parameter  $k_{carbsedshallow}$ .

## 6- Model Scenarios

Given the uncertainty in the absolute value of the seawater boron isotope composition (section S4), we consider two scenarios with initial steady-state conditions as in Table S6: scenario *CO<sub>2</sub>Hi* uses  $\delta^{11}B_{SW}=36.86$ , and *CO<sub>2</sub>Lo* uses  $\delta^{11}B_{SW}=34$ . Here ocean pH depends on the combination of atmospheric  $pCO_2$  and carbonate saturation state. Atmospheric  $pCO_2$  (set by the ratio of net carbon sources : silicate weatherability) is tuned to 3 or 10 PAL, encompassing the range of conditions considered by previous model studies (77, 78, 79). Ocean carbonate saturation state is set by carbonate sedimentation efficiency parameter  $k_{carbsedshallow}$ , which represents a combination of shelf area x deposition rate. A summary of scenarios required to explain the three events in our  $\delta^{11}B$  data are given in Table S7 and explored in further detail below.

705 Table S6 Steady-state initial conditions summary

	<b>CO<sub>2</sub>Hi</b>	<b>CO<sub>2</sub>Lo</b>	<b>Units</b>	<b>Description</b>
<b><i>Parameters</i></b>				
k <sub>12_ccdeg</sub>	11.80x10 <sup>12</sup>	11.80x10 <sup>12</sup>	mol CO <sub>2</sub> yr <sup>-1</sup>	degassing
k <sub>17_oxidw</sub>	5x10 <sup>12</sup>	5.92x10 <sup>12</sup>	mol C yr <sup>-1</sup>	oxidative weathering
k <sub>silw</sub>	2.40x10 <sup>12</sup>	6.60x10 <sup>12</sup>	mol CaSiO <sub>3</sub> yr <sup>-1</sup>	Silicate weatherability
k <sub>carbsedshallow</sub>	18.43x10 <sup>12</sup>	1.44x10 <sup>12</sup>	mol CaCO <sub>3</sub> yr <sup>-1</sup>	Marine carbonate burial efficiency
<b><i>Steady-state conditions</i></b>				
pCO <sub>2</sub> , ppm	2800	845		
T <sub>mean</sub>	22.18	14.94	<sup>0</sup> C	Global mean temp
T <sub>O(s)</sub>	28.7	21.44	<sup>0</sup> C	Ocean temp
Ω <sub>arag(s)</sub>	2.44	6.15		Aragonite saturation, 's' box
pH	7.51,7.46,7.07	8.02, 7.99, 7.60	Total scale	Ocean pH, 's', 'h', 'd'
DIC total	5.53x10 <sup>18</sup>	6.01x10 <sup>18</sup>	mol	
δ <sup>13</sup> DIC <sub>(s)</sub>	+3.32	+2.97	‰	
<b><i>Fluxes</i></b>				
f <sub>carbw</sub>	27.46x10 <sup>12</sup>	15.58x10 <sup>12</sup>	mol CaCO <sub>3</sub> yr <sup>-1</sup>	Carbonate weathering
f <sub>silw</sub>	6.80x10 <sup>12</sup>	7.72x10 <sup>12</sup>	mol "CaSiO <sub>3</sub> " yr <sup>-1</sup>	Silicate weathering
f <sub>ccdeg</sub>	11.80x10 <sup>12</sup>	11.80x10 <sup>12</sup>	mol CO <sub>2</sub> yr <sup>-1</sup>	Degassing
f <sub>mccb</sub>	34.26 x10 <sup>12</sup>	23.30x10 <sup>12</sup>	mol CaCO <sub>3</sub> yr <sup>-1</sup>	Marine carbonate burial

706

707 Table S7 Overview of scenarios

Event	Time	Scenario	
		CO <sub>2</sub> Hi	CO <sub>2</sub> Lo
		$\delta^{11}\text{B}_{\text{sw}}=36.86$	$\delta^{11}\text{B}_{\text{sw}}=34$
pH rise	252.25 Ma	Marine productivity increase	
	252.05 Ma	Carbonate sedimentation efficiency decrease	
		Pyrite deposition, Carbonate weathering increase	
$\delta^{13}\text{C}$ drop, stable pH	252.00 Ma	Land organic carbon burial decrease	
	251.95 Ma	Slow (~50kyr) isotopically light carbon addition.	
Acidification, $\delta^{13}\text{C}$ change	no	251.88 Ma	Rapid (10kyr) isotopically heavy carbon addition

708

709

### 710 *6.1 Mechanisms for pH rise*

711 The rise in  $\delta^{11}\text{B}$  at 252.05 Ma corresponds to a rise in pH from 7.5 to 8.0 for scenario CO<sub>2</sub>Hi,  
712 and from 8.0 to 8.3 for scenario CO<sub>2</sub>Lo. Given the major upheavals in the Earth system at the  
713 end-Permian, multiple mechanisms including changes in silicate and carbonate weathering,  
714 and marine changes in calcification and due to anoxia may potentially contribute to pH rise,  
715 and we use model sensitivity studies to determine potential constraints. We first review  
716 evidence for each mechanism, then summarize the model sensitivity studies and propose  
717 plausible scenarios involving multiple drivers.

### 6.1.1 Carbonate weathering

The overall high weathering rates across the Permian-Triassic boundary also imply an increase in carbonate weathering, possibly combined with any direct effect from chemical weathering of eroded clastic material itself.

There is also direct evidence for later sea-level regression and subaerial weathering of the shallowest sections of the S. China carbonate platform, coincident with EP1 (20) which may contribute to maintaining pH over this interval. To estimate an order of magnitude for enhanced carbonate shelf weathering:  $10^{18}$  mol  $\text{CaCO}_3$ , density  $2.8 \text{ g cm}^{-3}$  has volume  $36,000 \text{ km}^3$ , or  $100\text{m} \times 3.6 \times 10^5 \text{ km}^2$ , or  $1800\text{km}$  of  $200\text{km}$  wide shelf; this would provide a weathering flux of  $10^{13} \text{ mol CaCO}_3 \text{ yr}^{-1}$  for  $100 \text{ kyr}$ , comparable to the background carbonate weathering rate.

### 6.1.2 Decrease in calcification effectiveness

Overall global biotic calcification effectiveness is determined by the combination of available shelf area, and local ecosystem-dependent rates. A reduction in area of deposition could be because anoxic/euxinic waters extend onto the shelf bottom precluding those parts from hosting deposition, and/or because there is a sea level change reducing shelf area. The input of clastics prior to EP1 could also reduce carbonate production as a result of ecosystem impacts (80, 81).

### 6.1.3 Productivity-driven ocean anoxia, sulphate reduction, and pyrite burial

Multiple lines of evidence suggest a (large) expansion of oxygen minimum zones prior to the PT boundary, while the deep ocean remains suboxic. These include U isotope evidence for ~6x increase in anoxic fraction (82), extensive pyrite deposition (83), and GCM studies (84) illustrating the spatial distribution of anoxia.

We represent productivity-driven ocean anoxia by increasing marine phosphorus from the present-day value to 2.3x present (the value used by (66). This is achieved by adding phosphorus to the marine 's' reservoir (representing a net excess of riverine input over sediment output) at rate  $3.9 \times 10^{10} \text{ mol yr}^{-1}$  over the interval 252.15 – 252.05 Ma (cf present-day riverine input  $\approx 2 \times 10^{10} \text{ mol yr}^{-1}$ ) (64). This results in  $\text{pCO}_2$  drawdown as a result of the increased biological pump, and in sulphate reduction leading to  $\sim 50 \text{ } \mu\text{M H}_2\text{S}$  in the 'd' box. Note that sulphate reduction increases alkalinity / pH in the 'd' box by  $\Delta\text{pH} \sim 0.1$ , but as the S redox shuttle is completed by sulphide oxidation at the base of the oxic surface box, this has no effect on the pH of the oxic surface ocean.

High rates of pyrite formation are seen at and before EP1 (83, 85). Pyrite burial results in a net alkalinity source (86). We assume that pyrite deposition is a water-column process, hence is limited by the availability of iron and sulphide. The most limiting factor for the scenarios considered here is iron. To quantify this, we estimate pyrite deposition rate sustainable over a timescale of  $\sim 100 \text{ kyr}$  as  $\sim 1.25 \times 10^{12} \text{ mol FeS}_2 \text{ yr}^{-1}$ , based on availability of reactive iron  $\text{Fe}_{\text{HR}}$  (in the contemporary oxic ocean,  $\text{Fe}_{\text{HR}}$  total input to the ocean is  $\sim 6.8 \times 10^{12} \text{ mol yr}^{-1}$ , of which only  $\sim 1.3 \times 10^{12} \text{ mol yr}^{-1}$  gets to the deep ocean (87). Sulphide availability is determined by anaerobic organic carbon remineralisation in the 'd' box, which is a model-determined fraction of total export production  $\sim 10^{14} \text{ mol yr}^{-1}$ , and is less limiting than iron for the scenarios considered here. This assumes that sulphate for remineralisation (and hence sulphide availability) is unconstrained by marine sulphur availability, ie that the marine sulphate reservoir is drawn down. This is supported by (or at least consistent with) the data indicating low early Triassic marine sulphate,  $< 4 \text{ mM}$  (75, 88).

#### 6.1.4 Silicate weathering

Anomalously high sediment fluxes across the Permian-Triassic boundary (80, 81) imply soil loss and increased exposure of highly weatherable rock surfaces, with increases in both physical and chemical weathering. Early Siberian traps emplacement and an increase in area of weatherable basalt also may contribute to an increase in overall silicate weatherability. The main increase in silicate weathering is seen in the Griesbachian but increases may have accompanied the carbon injection for EP1.

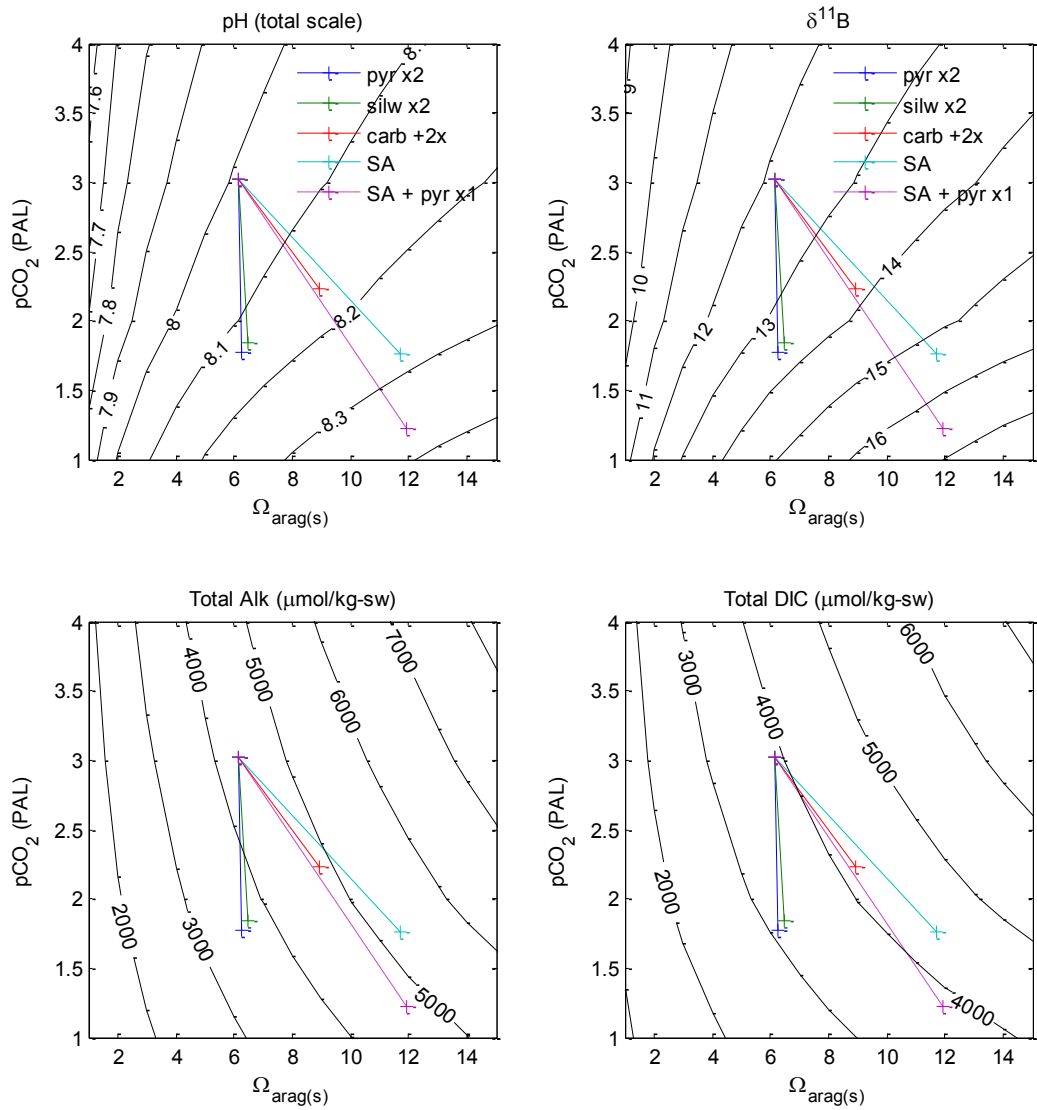
#### 6.1.5 Combined scenarios

We summarize the effect of illustrative perturbations for the separate contribution of each potential driver of pH increase in Table S8. Perturbations were applied to the CO<sub>2</sub>Lo steady state at 251.95Ma (corresponding to the pH rise seen in the  $\delta^{11}\text{B}$  data), with effect shown 100kyr later (at EP1). The marine carbonate system responds on a timescale of ~10kyr, hence reaches a steady state source-sink balance, however the timescale for land-surface weathering feedbacks is >~100 kyr hence the system does not reach a steady state. The dynamic response is included in the full scenarios.

As shown in figure S5, the perturbations fall into two groups. Increases in silicate weatherability and pyrite deposition leave carbonate input rate and calcification output essentially unchanged, hence result in changes to atmospheric pCO<sub>2</sub> at nearly constant saturation state. Changes to atmospheric pCO<sub>2</sub> alone are unable to produce a change in pH or  $\delta^{11}\text{B}$  as large as that seen in the data without implausibly low pCO<sub>2</sub> and hence temperature, hence these cannot be the sole drivers of pH increase. Reductions in calcification effectiveness or increases in carbonate inputs change both the carbonate system saturation state and atmospheric pCO<sub>2</sub>, resulting in a much larger increase in pH for a given decrease in pCO<sub>2</sub>. A major contribution from either or both of these mechanisms is therefore required.

The results from the perturbations study demonstrate that all mechanisms may contribute to pH rise, with a major contribution from either or both carbonate input and decrease in calcification effectiveness required. Given the most likely case where multiple mechanisms all contribute, we construct scenarios with a decrease in calcification effectiveness as the major component and smaller contributions from pyrite burial and carbonate weathering (Figure S6). The perturbations considered for the two scenarios are summarized in Table S9 and the dynamic response is shown in Figure S6.

798



799

Figure S5 Effect of illustrative perturbations (defined in Table S8) on carbonate system properties for atmosphere and ocean surface (s) box. Contours show carbonate system parameters for a constant temperature of 25 °C, salinity 35 psu, pressure 1 atm, hence do not exactly correspond to the full model results with varying temperature.

800

801

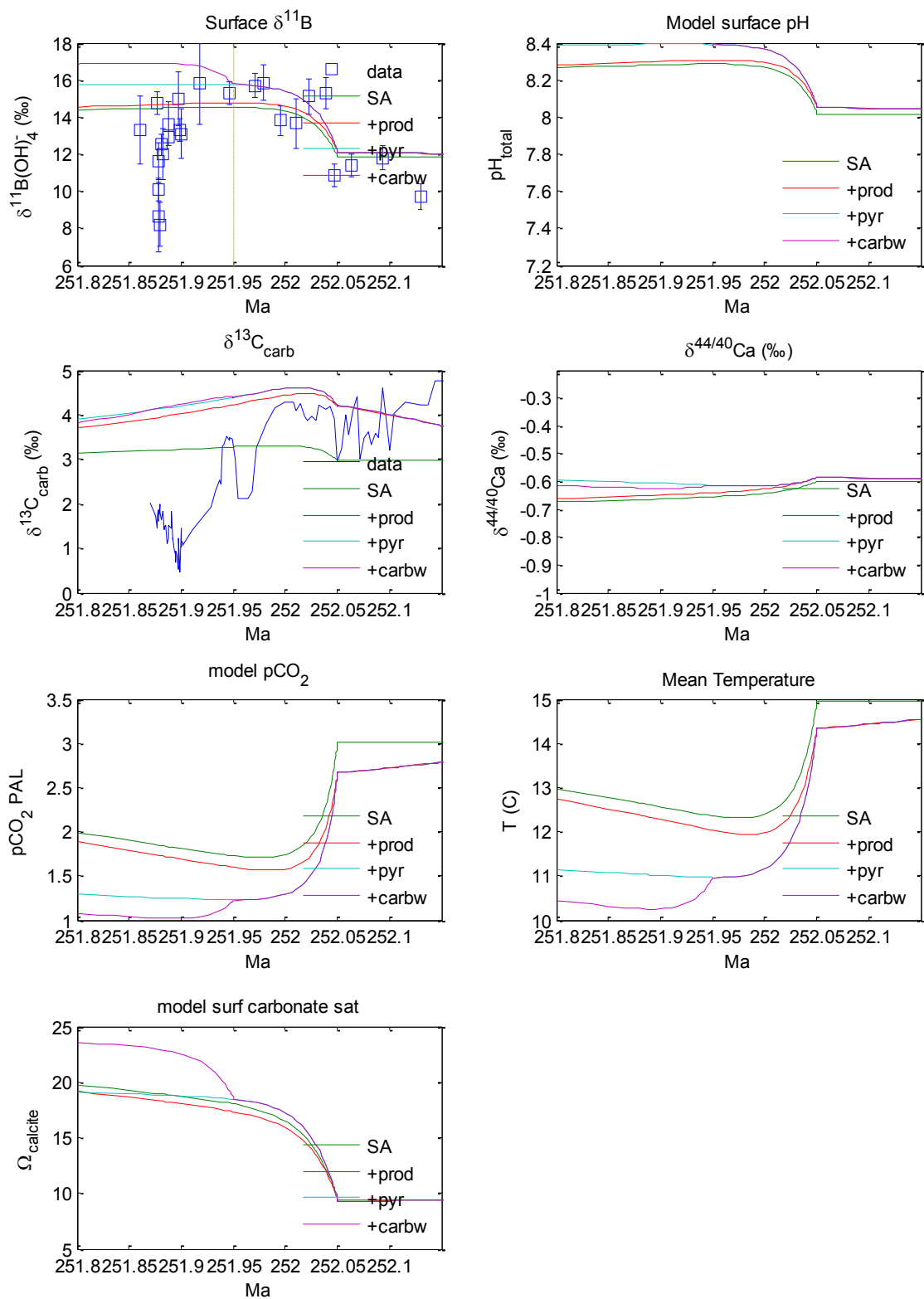


Figure S6 Scenario CO<sub>2</sub>Lo: Contributions to pH increase. 'SA': effect of calcification effectiveness decrease. '+prod' effect of increased marine productivity and anoxia. '+pyr' pyrite burial, and '+carb' carbonate weathering

Table S8 Sensitivity study for pH rise mechanisms. Perturbations applied to steady-state  $CO_2Lo$  at 252.05Ma, effect shown at 251.95Ma.

<b>Mechanism</b>	<b>Perturbation</b>	<b>pH<sub>tot(s)</sub></b>	<b><math>\delta^{11}B_{(s)}</math></b>	<b><math>\Omega_{arag(s)}</math></b>	<b>pCO<sub>2</sub></b>	<b>T<sub>mean</sub></b>	<b>Comments</b>
<i>steady-state</i>	none	8.02	11.83	6.15	845	14.94	<b>Error! Reference source not found.</b>
<b><i>CO<sub>2</sub>Lo</i></b>							
<hr/>							
<b><i>'calc eff'</i></b>	$K_{carbdsdshallow}$	$14.4 \times 10^{11}$	$\rightarrow$	+0.266	+2.72	+5.55	-351 -2.58
<b><i>decrease</i></b>	$2.47 \times 10^{11}$ (ie x 0.17)						
	$K_{carbdsdshallow}$	$14.4 \times 10^{11}$	$\rightarrow$	+0.36	+3.78	+8.2	-446 -3.39
	$1.23 \times 10^{11}$ (ie x 0.085)						
<b><i>pyr deposition</i></b>	'x1': $1.25 \times 10^{12}$ mol FeS <sub>2</sub> yr <sup>-1</sup>		+0.083	+0.71	-0.03		-213 -1.39
	'x2': $2.5 \times 10^{12}$ mol FeS <sub>2</sub> yr <sup>-1</sup>		+0.155	+1.36	+0.12		-347 -2.46
	'x4': $5 \times 10^{12}$ mol FeS <sub>2</sub> yr <sup>-1</sup>		+0.318	+3.062	+0.46		-557 -4.66
<b><i>carb input</i></b>	'+1x': add $15 \times 10^{12}$ mol CaCO <sub>3</sub> yr <sup>-1</sup>		+0.082	+0.77	+1.44		-130 -0.81
							~ upper limit from Fe availability +1x = approx 2x background weathering rate. Ocean carb deposition rapidly compensates +2x = ~3x background weath rate +3x = ~4x background weath rate
<b><i>silw increase</i></b>	'x2': add $30 \times 10^{12}$ mol CaCO <sub>3</sub> yr <sup>-1</sup>		+0.147	+1.41	+2.76		-219 -1.44
	'x3': add $45 \times 10^{12}$ mol CaCO <sub>3</sub> yr <sup>-1</sup>		+0.20	+1.97	+3.99		-285 -1.94
	'x2 k <sub>silw</sub> $6.60 \times 10^{12} \rightarrow 13.2 \times 10^{12}$		+0.14	+1.19	+0.35		-329 -2.30
	'x4 k <sub>silw</sub> $6.60 \times 10^{12} \rightarrow 26.4 \times 10^{12}$		+0.32	+3.08	+0.57		-588 -5.09
<b><i>calc eff + pyr</i></b>	$K_{carbdsdshallow}$	$14.4 \times 10^{11}$	$\rightarrow$	+0.37	+3.91	+5.78	-501 -3.98
	$2.47 \times 10^{11}$						
	'x1': $1.25 \times 10^{12}$ mol FeS <sub>2</sub> yr <sup>-1</sup>						
<b><i>carb + pyr</i></b>	'x2': add $30 \times 10^{12}$ mol CaCO <sub>3</sub> yr <sup>-1</sup>		+0.28	+3.09	+2.92		-485 -3.79
	'x2': $2.5 \times 10^{12}$ mol FeS <sub>2</sub> yr <sup>-1</sup>						

804

805

806 Table S9 Summary of pH rise mechanisms included in scenarios *CO<sub>2</sub>Hi* and *CO<sub>2</sub>Lo*

	<i>CO<sub>2</sub>Hi</i>	<i>CO<sub>2</sub>Lo</i>
Decrease in calcification effectiveness	$k_{\text{carbsedshallow}}$ decrease from $1.8433 \times 10^{13}$ to $0.72 \times 10^{12}$	$k_{\text{carbsedshallow}}$ decrease from $1.44 \times 10^{12}$ to $2.47 \times 10^{11}$
Productivity, anoxia	Increase P linearly to 2.3x, over interval 252.25 – 252.05 Ma	
Pyrite burial	$1.25 \times 10^{12}$ mol FeS <sub>2</sub> yr <sup>-1</sup> starting at 252.05Ma	
Carbonate weathering	$9.7 \times 10^{12}$ mol/yr starting at 251.95Ma	

807

808

809

## 6.2 Sources of carbon and volatiles causing a negative $\delta^{13}\text{C}$ excursion or pH excursion

### 6.2.1 Terrestrial Carbon burial

The effect of destruction of the land biota and a corresponding decline in land organic carbon burial at the PT boundary was first considered by Broecker and Peacock (89). We represent this by setting land organic carbon burial to zero at  $T=251.95\text{Ma}$ , resulting in a drop in  $\delta^{13}\text{C}_{\text{carb}}$  of  $\approx 4\text{‰}$  (comparable to that seen in end-Permian sections), but over timescale of  $\sim 100\text{kyr}$ .

### 6.2.2 Marine Carbon burial

Despite (or because of) ecological shifts to a cyanobacteria dominated ecosystem (3), proxy evidence for continued high sediment organic carbon fluxes (84) and a vertical  $\delta^{13}\text{C}$  gradient (92, 93) as well as continuing marine anoxia suggests that high marine productivity continues through Permian-Triassic. Interruption to the marine biological pump would result in a short timescale (ocean circulation timescale  $\sim 10^3\text{ yr}$ ) increase in surface ocean pH and decrease in surface ocean (and hence carbonate)  $\delta^{13}\text{C}$ . This was considered as a mechanism for short-timescale  $\delta^{13}\text{C}$  fluctuations over the PT interval (67). We do not consider this further here as this mechanism results in coupled perturbations to both surface ocean pH and  $\delta^{13}\text{C}$ , and hence cannot be the major driver for the ' $\delta^{13}\text{C}$  without pH' or 'pH without  $\delta^{13}\text{C}$ ' signals. Smaller perturbations (interruptions) to the biological pump may be plausible as a contributor to short-timescale  $\delta^{13}\text{C}$  signals following EP1.

### 6.2.3 *Siberian traps volcanism and contact metamorphism*

In order to bound plausible model scenarios, we review here potential mechanisms for volatile input from the Siberian Traps and summarise constraints on magnitudes and rates, based on (24, 27, 93).

The Siberian Traps magma area is estimated as  $2.5 - 5 \times 10^6 \text{ km}^2$  and volume  $> 2 \times 10^6 \text{ km}^3$ . This intruded into the Tunguska sedimentary sequence, which reaches 12.5 km in thickness and includes  $\approx 2.5 \text{ km}$  of Cambrian evaporites containing abundant limestone, halite, dolomite and anhydrite (24, 27), coal deposits, as well as Neo-Proterozoic petroleum-bearing shale and carbonate. Intrusion of magma into the sediments resulted in abundant sills and dykes with accompanying contact aureoles, and explosively-generated pipes. The igneous province is estimated to contain approximately 50% intrusive dykes and sills, 30% basalt lava flows, and 20% pyroclastic material (94, 95).

The volume of sediments affected by contact metamorphism is estimated (27) from a sill area of  $2 \times 10^6 \text{ km}^2$ , thickness 200m, generating a contact aureole of thickness 400m. This results in potential release of  $0.8 - 2.3 \times 10^{18} \text{ mol C}$  (as isotopically light methane and  $\text{CO}_2$ ) from metamorphic degassing of organic carbon (assuming the TOC weight percent reacted is 0.5 – 1.5%), over a timescale  $\approx 50 \text{ kyr}$ . In addition, pipes (each with source region  $\approx 5 \text{ km}^3$ ) could release  $0.1 - 0.3 \times 10^{18} \text{ mol C}$  over  $\approx 6.5 \text{ kyr}$ . Intrusion into carbonates could release comparable quantities of isotopically-heavy  $\text{CO}_2$  via calcsilicate formation and decarbonation of dolomite into periclase and calcite, and intrusion into anhydrite could release comparable quantities of S as  $\text{SO}_2$  (96). Interaction between petroleum-bearing inclusions and host rock salt could in addition generate halocarbons, estimated at  $1 - 3 \times 10^{17}$

mol CH<sub>3</sub>Cl (35). Intrusion into coal-seams could result in explosive interaction resulting in large-scale coal combustion (93).

The Siberian Traps magmas contain anomalously high quantities of S, Cl, F (27), estimated to result in total intrusive and extrusive degassing of 0.2-0.25x10<sup>18</sup> mol S, 0.1-0.25 x10<sup>18</sup> mol Cl, and 0.4-0.7 x10<sup>18</sup> mol F (31). The ultimate source of these volatiles is likely to be assimilation from sedimentary host rocks.

#### 6.2.4 Carbon injection perturbations

Given the episodic nature and likely variability in isotopic composition of carbon additions from Siberian Traps volcanism and contact metamorphism, we consider size, rate, and isotopic composition of carbon additions via sensitivity studies within plausible ranges.

The effect on  $\delta^{13}\text{C}_{\text{carb}}$  of a carbon addition of isotopic composition  $\delta^{13}\text{C}_{\text{carb}}$  is given approximately by mass-balance with the surface (atmosphere and ocean) carbon reservoirs (78, 79). The effect on pH is additionally dependent on the rate of addition. We show in Table S10 model results for combinations of addition size, isotopic composition and rate, constrained to result in  $\delta^{13}\text{C}_{\text{carb}} = -3 \text{ ‰}$ , demonstrating the additional non-linear effect of land-surface weathering feedbacks ('land carbonate compensation').

The decline in  $\delta^{13}\text{C}_{\text{carb}}$  over the P-T boundary is faster than can be accounted for by a decrease in land carbon burial alone, implying an additional pulse of isotopically light carbon contribution  $\sim 2\text{‰}$  to the decline. We show in Figure S7 the constraints from the  $\delta^{11}\text{B}$  data on carbon additions over the 50kyr interval 251.95 – 251.90 Ma. The results demonstrate that providing the rate of carbon addition is relatively slow as here, the pH

constraints are in fact relatively weak, and are consistent with a range of input isotopic compositions  $\delta^{13}\text{C}_{\text{inj}}$ .

Table S10 Carbon injection perturbations, constrained to result in  $\delta^{13}\text{C}_{\text{carb}} = -3 \text{ ‰}$  when applied to steady-state condition  $\text{CO}_2\text{Lo}$

Size (mol C)	Duration	Rate (mol / yr)	$\delta^{13}\text{C}_{\text{inj}}$	$\Delta \text{pH}$
$4.75 \times 10^{17}$	$10^5 \text{ yr}$	$4.75 \times 10^{12}$	-50	-0.07
$2.47 \times 10^{18}$	$10^5 \text{ yr}$	$2.47 \times 10^{13}$	-10	-0.28
$3.32 \times 10^{17}$	$10^4 \text{ yr}$	$3.32 \times 10^{13}$	-50	-0.18
$1.75 \times 10^{18}$	$10^4 \text{ yr}$	$1.75 \times 10^{14}$	-10	-0.64

The acidification event at  $\sim 251.89 \text{ Ma}$  requires a rapid addition of carbon on a timescale  $\leq 10 \text{ kyr}$ , with an isotopic composition  $\delta^{13}\text{C}_{\text{inj}} \approx 0 \text{ ‰}$  in order to leave  $\delta^{13}\text{C}_{\text{carb}}$  unaffected, and size  $\geq 2 \times 10^{18} \text{ mol}$  in order to produce a sufficient decline in pH and  $\delta^{11}\text{B}$  (Figure S8). Larger (or more rapid) carbon additions produce relatively little additional response in ocean pH, as the majority of the input carbon remains in the atmosphere, and the response of the  $\delta^{11}\text{B}$  is also non-linear at low pH. The rate of the inferred carbon addition is  $\sim 3$  times the estimates above for organic carbon from the combined effects of sills ( $0.16 - 0.4 \times 10^{18} \text{ mol C}$  over  $10 \text{ kyr}$ ) and pipes ( $0.1 - 0.3 \times 10^{18} \text{ mol C}$  over  $\sim 6.5 \text{ kyr}$ ), but is not unreasonable given the carbonate carbon source and large uncertainties in these estimates.

#### 6.2.5 $\text{SO}_2$ injection perturbation

Contact metamorphism of evaporites resulting in large  $\text{SO}_2$  release could potentially also contribute to the acidification event. Quantitatively the effect (per mol) on ocean pH is

894 approximately twice that of a carbon addition, and given the relative abundance of  
895 evaporites to carbonates is therefore likely to represent a smaller contribution to  
896 acidification.

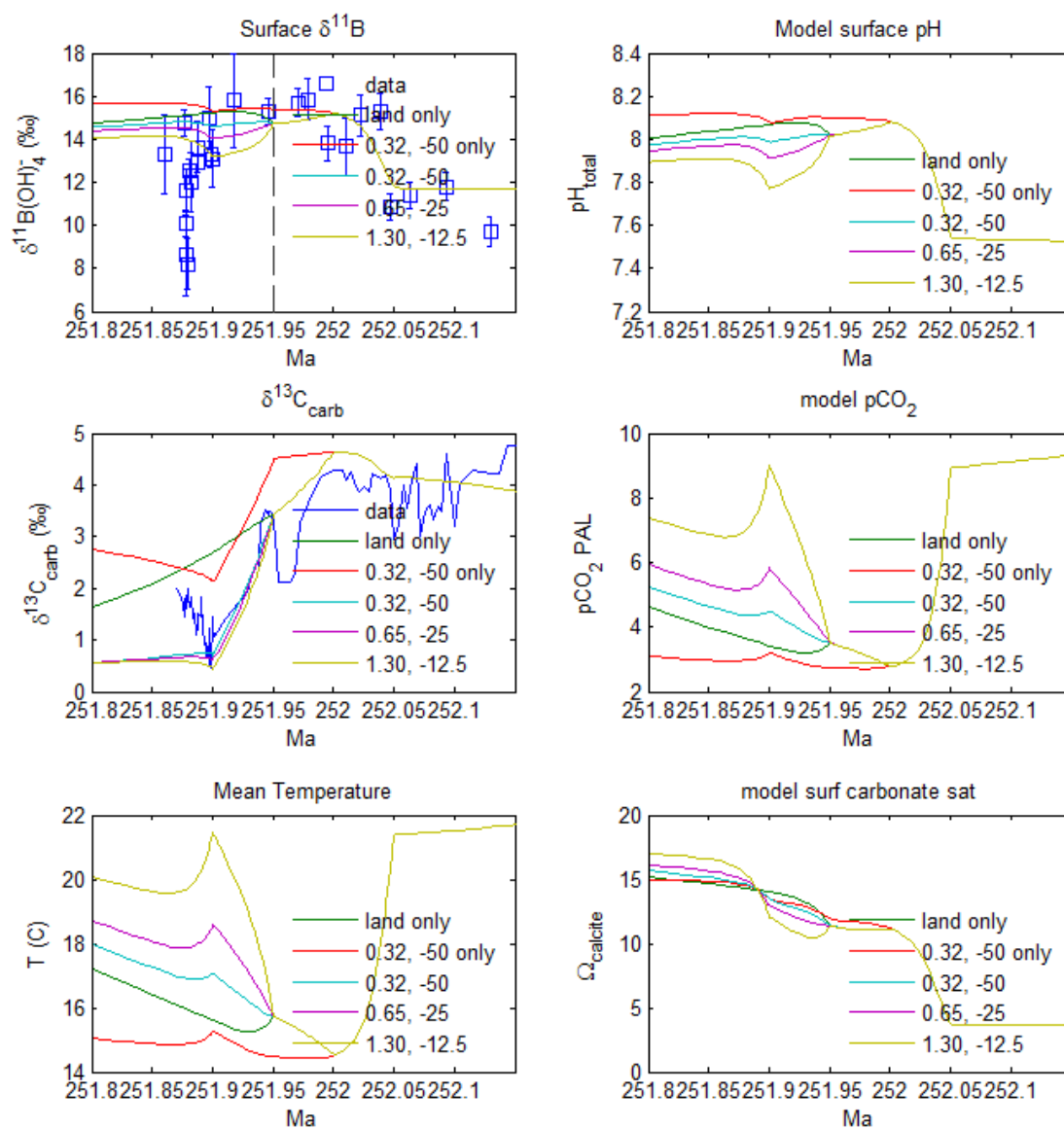


Figure S7 Effect of changing size and isotopic composition of CO<sub>2</sub> input perturbations applied to scenario *CO<sub>2</sub>Hi* over 50kyr interval 251.95 – 251.90 Ma. 'land only' shows the effect of interruption in land organic burial, '0.32, -50 only' shows the effect of carbon addition only. Other lines show combined effect of land burial and carbon addition. Perturbations are constructed to result in  $\delta^{13}\text{C}_{\text{carb}} \approx -2$  ‰, and correspond to inputs of:  $0.32 \times 10^{18}$  mol / -50 ‰;  $0.65 \times 10^{18}$  mol / -25 ‰;  $1.30 \times 10^{18}$  mol / -12.5 ‰

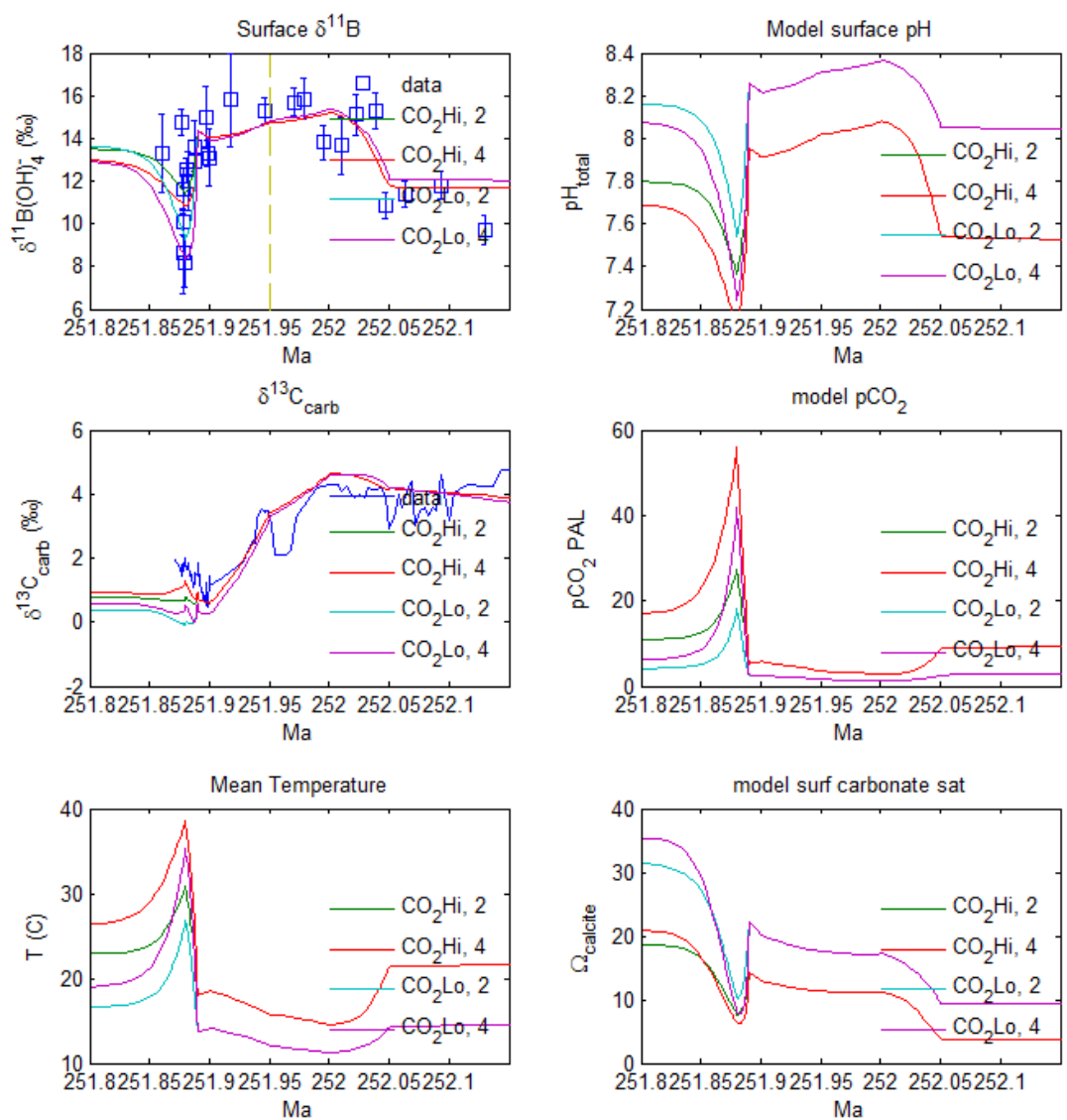


Figure S8 Effect of changing size of CO<sub>2</sub> input perturbations applied to scenarios *CO2Hi* and *CO2Lo* over 10kyr interval 251.89 – 251.88 Ma. Perturbation sizes are 2x10<sup>18</sup> mol and 4x10<sup>18</sup> mol. Isotopic composition is 2.65 ‰, ie equal to that of sedimentary carbonate.

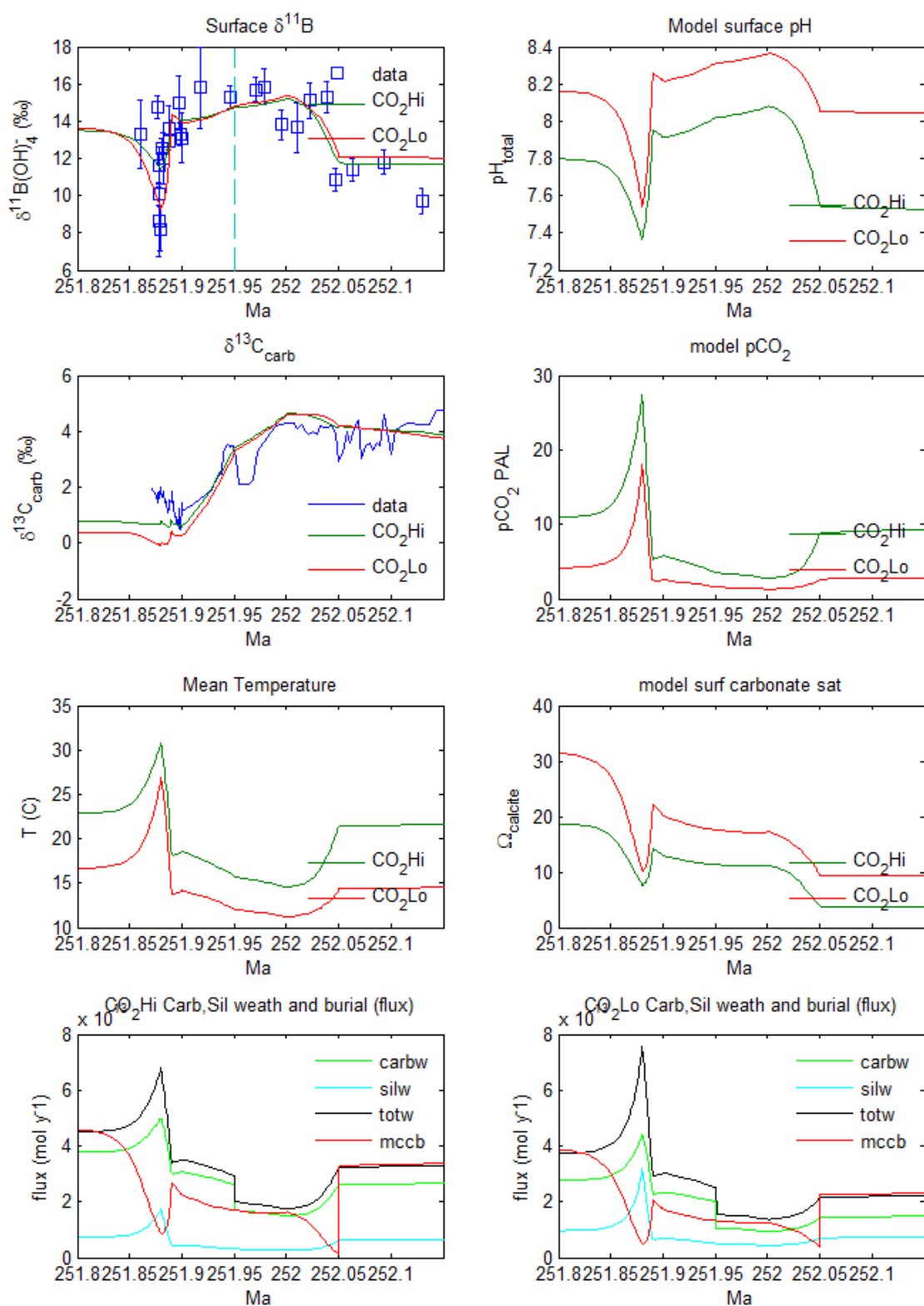


Figure S9 Additional model output for CO<sub>2</sub> scenarios shown in main paper Figure 3. Weathering fluxes are shown for scenario CO<sub>2</sub>Lo only.